Development of a Miniature, Semi-Distributed Sapphire Fiber Optic Thermometer for Harsh and High Temperature Environments

Keith Alan DePew

Thesis submitted to the faculty of the Virginia Polytechnic Institute and State University in partial fulfillment of the requirements for the degree of

Master of Science
In
Electrical Engineering

Anbo Wang, Committee Chair
Kathleen Meehan
Yong Xu

December 4, 2012
Blacksburg, VA

Keywords: Thermometer, high temperature, distributed, harsh environment, sapphire, Fabry-Perot, interferometer, nano-fabrication

Copyright 2012, Keith DePew

Development of a Miniature, Semi-Distributed Sapphire Fiber Optic Thermometer for Harsh and High Temperature Environments

Keith DePew

ABSTRACT

Fiber optic temperature sensing has become a well-defined field in the past few decades [1] through the use of Fiber Bragg Gratings, Fabry-Perot interferometry, and pyrometry, to list several techniques in use today. The use of fiber optics offers significant advantages over electronic sensing in terms of size and insensitivity to harsh conditions such as extreme temperatures and corrosive environments. The availability of optical sapphire materials, including fibers, has allowed the creation of fiber optic sensing elements able to continuously operate at temperatures of 1600°C [2] or more, thus outstripping the abilities of many commonly used thermocouples (excluding platinum types R, S, and B) [3] which will also exhibit a sensitivity to electromagnetic fields.
In addition to the aforementioned benefits, fiber optic sensing techniques provide a great deal of accuracy in temperature measurement over the entire working range of the sensor.

The work documented in this thesis consists of efforts to minimize the overall footprint of a sapphire based extrinsic Fabry-Perot interferometry (EFPI) temperature sensing element, as well as strides made in multiplexing the same element and reducing the error potential from cross sensitivity of the thermometer with applied strain. This work has been variously funded by Pratt & Whitney and the Department of Energy.

ACKNOWLEDGEMENTS

First and foremost, I would like to thank Dr. Anbo Wang, my advisor, for providing me the opportunity to engage in my graduate studies with the Center for Photonics Technology (CPT). Dr. Wang's confidence and support, beginning with our very first meeting, has sustained and driven me to succeed during my tenure with the CPT. It was a pleasure to be led by such a first rate scientist and laboratory director, whose academic expertise and devotion to excellence is matched by his ability to engage on both a personal and professional level with his students and peers. His demonstration of character is one I shall not forget. I would also like to thank my committee members, Dr. Kathleen Meehan and Dr. Yong Xu for both their tutelage and support during my graduate studies.

Thanks are also due to my project managers: Firstly, Dr. Evan Lally, whose guidance during my initial foray into fiber optic sensing has proven invaluable, and whose patience during my initial learning curve knew no bounds. Thanks to Dr. Bo Dong for his assistance and practical knowledge which has been invaluable time and again. And lastly, but certainly not least, Dr. Cheng Ma, whose demonstration of excellence in both theoretical and practical engineering will continue to stand as an example to strive for.

All of the members of the CPT family also deserve my thanks, in particular Tyler Shillig, Dorothy Wang, Zhipeng Tian, Michael Fraser, Chennan Hu, Bo Liu, and Brian Scott, for their support and assistance over the past two years.

Several members, both current and former, of the Nano-scale Characterization and Fabrication Laboratory deserve special mention for their tutelage, guidance, and assistance during the nano-fabrication phase of the project. Foremost among them is Dr. Jim Schiffbauer without whom I would never even have thought it possible to pursue nano-fabrication techniques for EFPI sensors. Thanks also to Dr. Jerry Hunter for his expertise and instruction, and to Jay Tuggle and Andrew Giordino for their assistance throughout the laboratory.

A word of thanks also to my friends in the Geology department who kept me grounded during my graduate studies. A big thank you to Christina Blue, whose friendship, encouragement, and occasional reprimand kept my research moving forward even when I didn't feel I had the will. Your support will not be forgotten.

Thanks also to my sponsors, Pratt & Whitney and the Department of Energy (DOE), for their support of my research. I hope that my work will reflect well on their generous contribution to the engineering sciences at Virginia Tech.

And the biggest thanks to my wife for her unwavering support during these long years that I have been away. Her encouragement and understanding is immeasurable, and I could not have finished this work without her. There are not words to convey the gratitude that I have for all she has endured in my absence.

Table of Contents

Chapter 1: Introduction **1**

1.1 Introduction to Optical Fiber 1

1.2 Temperature Sensing Methods 5

1.2.1 Mechanical Temperature Sensors 5

1.2.2 Electrical Temperature Sensors 5

1.2.3 Optical Temperature Sensors 6

1.3 High Temperature Optical Sensor Selection 8

1.4 Thesis Topic Organization 9

Chapter 2: Sensing Method Principles **10**

2.1 Fabry-Perot Interferometry 10

2.2 Basic System Setup 14

2.2.1 Sensing Element 15

2.2.2 Light Injection System 15

2.2.3 Spectrometer Options 16

2.3 Basic System Signal Processing 17

Chapter 3: Sensor Interrogation and Evaluation **19**

3.1 Determination of Cavity Distance 19

3.2 Sensing Element Quality 21

3.2.1 Fringe Visibility 21

3.2.2 Etalon Quality Control 24

3.2.3 Etalon Length 27

Chapter 4: Fabrication of Sensing Elements **29**

4.1 Wafer Etalon Design 29

4.1.1 Slot and End Sensor Designs 29

4.1.2 Strain Cross Sensitivity Testing 31

4.1.3 Sensor Head Temperature Resolution 35

4.1.4 Strain Cross-Sensitivity Conclusions 37

4.1.5 Adhesive Ferrule Design 38

4.2 Focused Ion Beam Fabrication 40

4.2.1 FIB Nano-fabrication Overview ... 40
4.2.2 Wafer Milling ... 41
4.2.2.1 Fiber Wafer Milling Conclusions ... 45
4.2.3 Nano-structure Cavities ... 46
4.2.3.1 Milled Cavity Interferometer ... 46
4.2.3.2 Modal Interference ... 53
4.3 Direct Bonding of Sapphire Fibers ... 56
4.3.1 Direct Bonding Analysis ... 59
Chapter 5: Sensor Multiplexing ... 60
5.1 Multiplexing the Wafer Etalon Design ... 60
Chapter 6: Summary and Recommendations for Future Work ... 63
6.1 Work Summary ... 63
6.2 Recommendations for Future Work ... 63
References ... 64

List of Figures

Figure 1-1: Section view of the basic fiber optic structure showing the core and surrounding cladding…………………………………………………………………………..1

Figure 1-2: Diagram of light rays encountering an air water interface……………………………….2

Figure 1-3: Plot of V-number versus propagation constant for several common LP modes………………………………………………………………………………………………4

Figure 1-4: Optical power distribution of common LP modes………………………………………..4

Figure 1-5: Ray trace diagram illustrating the difference in path length and internal reflection angle of higher and lower order modes……………………………………5

Figure 1-6: Blackbody spectral radiance of electromagnetic radiation at various temperatures………………………………………………………………………………..7

Figure 2-1: Examples of wavelengths that are in phase versus wavelengths that are out of phase by Pi radians………………………………………………………………………10

Figure 2-2: Diagram of a Fabry-Perot etalon where theta is the angle of incidence…………..11

Figure 2-3: Sketch of the ray paths involved in the calculation of optical path difference between two consecutive transmitted rays…………………………………………..12

Figure 2-4: Plot of etalon optical power transmission/reflection by wave……………………..12

Figure 2-5: Plot of cosine of phase delay experienced by a ray reflected by a Fabry-Perot cavity of arbitrary length versus wavelength……………………………………….14

Figure 2-6: Schematic diagram illustrating the major components of the Fabry-Perot optical thermometer system set up for this project……………………………………..14

Figure 3-1: Plot of the Fourier transform of an interference pattern obtained from a sapphire wafer showing the signal peak corresponding to the wafer cavity sensed……………………………………………………………………………………………..20

Figure 3-2: Plot of an ideal interference pattern for an interferometer which experiences no losses and no noise……………………………………………………………………22

Figure 3-3: Interference pattern generated by a sapphire wafer interrogated with a fiber………………………………………………………………………………………………23

Figure 3-4: A schematic diagram of non-parallel etalon surfaces where the effect of delta-d acts to increase the path length experienced by the right hand ray as compared to the left hand ray when reflected between the two surfaces……24

Figure 3-5: Plot of fringe visibility as a function of wedge angle between the Fabry-Perot etalon's reflective surfaces……………………………………………………………………25

Figure 3-6: Newton Rings formed by the differential thickness of the sapphire wafer modulating the interference pattern of a 650 nm illuminating laser……..……25

Figure 3-7: Diagrams of specular and diffuse reflection ray traces resulting from incident light impinging on two surfaces of different roughness……………….…………..26

Figure 3-8: Hand polishing sapphire wafers was accomplished using a polishing platen to maintain wafer parallelism on a polishing wheel……………………………………26

Figure 3-9: Plot of fringe visibility as a function of gap length………………………..…………..27

Figure 3-9: Plot of the number of fringes visible in a 200 nm bandwidth as a function of cavity length………………………………………………………………………………………28

Figure 4-1: Cutaway representation of the end sensor and slot sensor designs utilized for Extrinsic Fabry-Perot Interferometric temperature sensing……………………30

Figure 4-2: Strain cross-sensitivity testing plate sensor schematic indicating locations of two fiber sensors and foil strain gauge………………………………..……………31

Figure 4-3: Strain cross-sensitivity testing apparatus…………………………………………...33

Figure 4-4: Plot of applied strain as a function of the deflection distance of the tip of the strain plate……………………………………………………….…………………………..33

Figure 4-5: Optical path difference of slot sensor wafer etalon as measured at incremental applied strains……………………………………………………………………..…………..34

Figure 4-6: Optical path difference of end sensor wafer etalon as measured at incremental applied strains……………………………………………………..…………………34

Figure 4-7: Variation in optical path difference of wafer etalon in slot sensor over time during a zero strain calibration run…………………………………………………..35

Figure 4-8: Variation in optical path difference of wafer etalon in end sensor over time during a zero strain calibration run…………………………………………………..36

Figure 4-9: Variation in the recorded optical path difference of a slot sensor and thermocouple temperatures over time during a zero strain calibration run……………………………………………………..……………………………..………..37

Figure 4-10: Variation in the recorded optical path difference of an end sensor and thermocouple temperatures over time during a zero strain calibration run……………………………………………………………………………………………37

Figure 4-11: Images of an adhesive ferrule design sensor head before and after introduction of Cotronic 989F alumina adhesive to the silica tube……………39

Figure 4-12: Optical interference patterns recorded for an adhesive ferrule sensor head prior to adhesive introduction, during adhesive curing, and after the adhesive has fully air cured………………………………………………………………………39

Figure 4-13: Sputter coating glass slides with affixed sapphire fibers with gold-palladium ensures a conductive path to dissipate excess charge buildup during focused ion beam imaging and patterning……………………………………………………42

Figure 4-14: Secondary electron image of sapphire fiber that has been partially cut using the gallium ion beam……………………………………………………………………43

Figure 4-15: Secondary electron image of sapphire fiber milled with a gallium ion beam………………………………………………………………………………………………44

Figure 4-16: Optical microscope image taken through the base of a sapphire fiber that had been milled with a gallium ion beam in an attempt to sever 50 microns off of the end……………………………………………………………………………………………45

Figure 4-17: Schematic representation of fiber tip cavity sensor showing a cross section view of the cavity at the fiber's end……………………………………………………46

Figure 4-18: Sapphire fibers mounted on vacuum chamber stage prior to focused ion beam milling……………………………………………………………………………………………47

Figure 4-19: Helios NanoLab vacuum chamber internal camera image of stage tilted to 52 degrees………………………………………………………………………………………47

Figure 4-20: A sapphire fiber that was in the process of being milled when the aluminum angle sagged under its own weight and caused a shift in the pattern placement relative to the fiber tip……………………………………………………48

Figure 4-21: A fiber clamp fabricated by Dr. Scott is fastened into the translation stage via a set screw holding the clamp's post……………………………………………………49

Figure 4-22: Three dimensional representation of wafer cavity edge imaged using an Atomic Force Microscope………………………………………………………………50

Figure 4-23: Optical image of cavity milled into a sapphire fiber using the ion beam……….50

Figure 4-24: Atomic Force Microscopy topography map of center of an ion beam milled cavity in a sapphire wafer……………………………………………………………………51

Figure 4-25: Secondary electron image of a 30 micron diameter by 12 micron deep cavity milled into the tip of a 75 micron diameter sapphire fiber………………………..52

Figure 4-26: Optical spectrum captured by an optical spectrum analyzer formed by the interrogation of a 30 micron diameter cavity milled sapphire fiber illuminated with a Super Continuum light source……………………………………..53

Figure 4-27: Optical interference spectrum and corresponding Fourier transform derived from the interrogation of a 32 micron thick sapphire wafer with a sapphire milled with a 30 micron diameter cavity of approximately 12 microns in depth…………………………………………………………………………………………………....54

Figure 4-28: Optical interference spectrum and corresponding Fourier transform derived from the interrogation of a 1 mm thick glass slide with a sapphire milled with a 30 micron diameter cavity of approximately 12 microns in depth…………………………………………………………………………………………………54

Figure 4-29: Ray trace diagram of a milled fiber tip's reflective surfaces with respect to two modes………………………………………………………………………………………………...55

Figure 4-30: Ray trace diagram of two modes in a fiber with a milled tip used to interrogate a thin etalon…………………………………………………………………………………55

Figure 4-31: Secondary electron image of a deep cavity milled into a 100/140 multimode silica fiber using the ion beam……………………………………………………………...56

Figure 4-32: Fume hood set-up of Nano-Strip solution, hot nitric bath, and sulfuric acid wash in preparation for fiber cleaning in the Whittemore Hall clean room…58

Figure 4-33: Excessive oxidation on low carbon steel components of alignment jig as a result of the high temperature bake…………………………………………………….58

Figure 4-34: Plot of the estimated misalignment angle of fibers in direct bonding alignment jig as a function of joint position in the ferrule……………………………………59

Figure 5-1: Cutaway representation of a multiplexed 3 sensor link of sapphire wafer sensing elements………………………………………………………………………………..60

Figure 5-2: A multiplexed 3 sensor link of sapphire wafer sensing elements illuminated with a 630 nm laser………………………………………………………………………………61

Figure 5-3: Plot of the Fourier transform derived from the combined interference patter generated by the three wafer etalons in multiplexed sensor link……………………………………………………………………………………………………..61

List of Tables

Table 4-1: A comparison of the coefficients of thermal expansion for the materials used to construct the sensor elements..30
Table 4-2: Strain cross-sensitivity and calculated temperature measurement error for each sensor geometry...38

Chapter 1: Introduction

1.1 Introduction to Optical Fiber

Following on the 1870 discovery by British physicist John Tyndall that light will be carried by a stream of water emerging from a container, research began in the 1950s to develop glass fibers to guide light [4]. Optical fibers opened the door to many new technologies, among which optical signal delivery was an important application. With the advent of low loss optical fibers first demonstrated in the 1970s (where low loss was initially considered to be 16 dB/km) it became obvious that optical signal delivery systems would quickly outpace existing wire-communications links by virtue of their longer distance runs between required repeating stations. This, in turn led to modern optical fibers with losses less than 3 dB/km at a wavelength of 850 nm, and even lower for longer wavelengths [5]. Today Corning's ClearCurve OM2 fiber advertises a loss of ≤0.6 dB/km at a wavelength of 1300 nm [5].

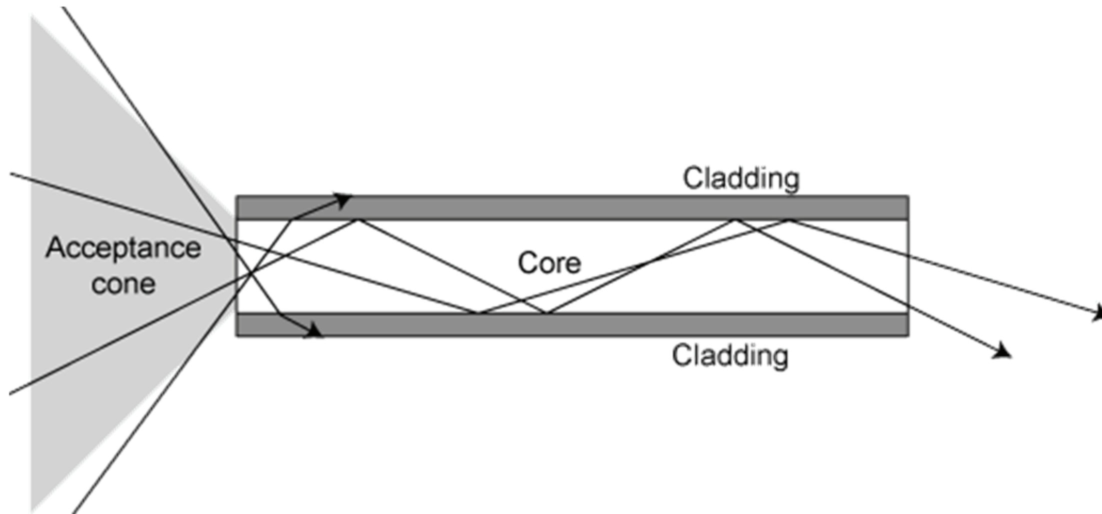

Figure 1-1: Section view of the basic fiber optic structure showing the core and surrounding cladding. Ray traces show modes which enter the fiber within the angle of the acceptance cone propagating while higher order modes do not (courtesy pacificcable.com)

Modern optical fiber, in its basic form, consists of a fiber core surrounded by a cladding, which has a lower index of refraction (Figure 1-1). In the case of Tyndall's water guided light, air composed the "cladding" layer where the index of refraction is smaller than that of the water "core". The change in index of refraction from the core to the cladding allows for the phenomenon of total internal reflection within the fiber. The angle at which total internal

reflection occurs is called the critical angle (Figure 1-2). The angle is dependent on the indices of refraction of the core and cladding of the fiber. This angle is given by Snell's law (Equation 1-1) where Θ_i is the angle of incidence (measured from the normal to the refractive face), Θ_r is the angle of refraction or reflection, n_1 is the index of refraction of the core, and n_2 is the index of refraction of the cladding.

$$n_1 \sin \theta_i = n_2 \sin \theta_t \tag{1-1}$$

Rearranging Equation 1-1 we obtain the incidence as Equation 1-2. We can solve for the critical angle, Θ_c, by evaluating the value of Θ_i when $\Theta_t = 90°$ (Equation 1-3).

$$\sin \theta_i = \frac{n_2}{n_1} \sin \theta_t \tag{1-2}$$

For any ray entering the fiber at an angle greater than the critical angle total internal reflection (TIR) will be observed and the ray will be propagated along the fiber.

$$\theta_c = \theta_i = \sin^{-1}\left(\frac{n_2}{n_1}\right) \tag{1-3}$$

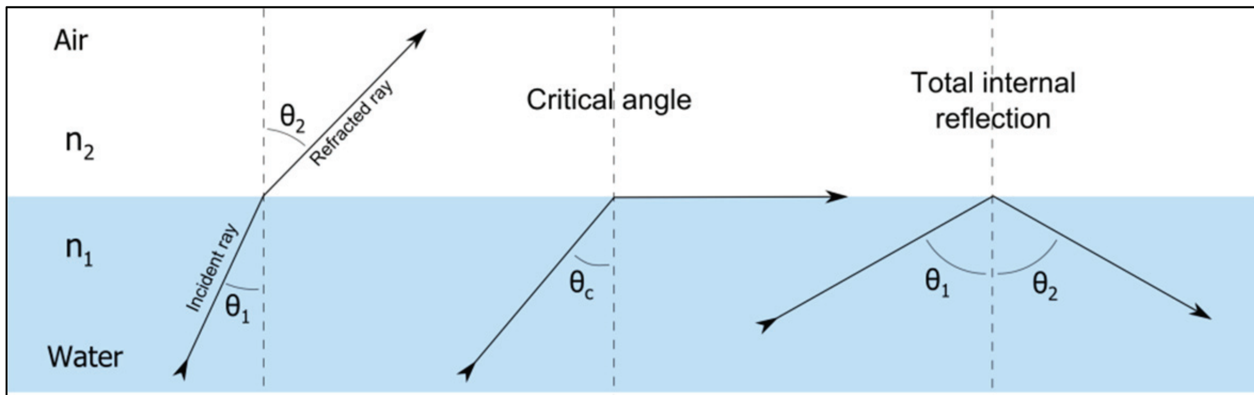

Figure 1-2: Diagram of light rays encountering an air water interface. Rays travelling from the water to the air are meeting a lower index of refraction in the air. At the critical angle, the rays become evanescent, and at greater incidence angles TIR occurs

For most fibers, the cone of acceptance for light to enter the fiber is given by the numerical aperture (NA) of the fiber. The NA of a particular fiber can be calculated using Equation 1-4, where Θ_{max} is the half angle of the acceptance cone as measured from the fiber's axis, n_1 is the index of refraction of the core, n_2 is the index of refraction of the cladding, and n is the index of refraction of the medium from which the light is entering the fiber (generally assumed to be air with an index of refraction of 1).

$$\mathrm{NA} = n\sin\theta_{max} = \sqrt{{n_1}^2 - {n_2}^2} \tag{1-4}$$

The physical design of the fiber's core also gives rise to distinguishing the fiber as either single or multimode. In single mode fibers, only one light ray path is permitted to propagate, while in multimode many paths, or modes, are permitted. This effect is driven by the physical dimensions of the core of the fiber as well as the composition of the core and cladding. For the basic fiber design discussed earlier, the diameter of the core and the indices of refraction of the core and cladding can be used to determine whether the fiber will be single or multimode for a certain wavelength of light by calculating the normalized frequency [6], V (also known as the V-number). The calculation of V is shown in Equation 1-5 where *a* is the radius of the core and λ is the wavelength of injected light in a vacuum.

$$V = \frac{2\pi a}{\lambda} NA = \frac{2\pi a}{\lambda}\sqrt{{n_1}^2 - {n_2}^2} \tag{1-5}$$

Fibers with a V-number of less than 2.4048 will only guide one ray path and are thus termed single-mode fibers. Multimode fibers will have a V-number greater than 2.4048 and will guide multiple modes. As the V-number increases to values significantly larger than 2.4048, the number of modes can be estimated as half of the square of the normalized (Equation 1-6).

$$Number\ of\ Modes \approx N \approx \frac{V^2}{2} \quad (for\ V \gg 2.4048) \tag{1-6}$$

Figure 1-3 shows the "V-number vs. *b* curve", which illustrates the V-number required for some common modes. The ordinate axis in this figure is given by the normalized modal propagation constant, *b*, which is defined in Equation 1-7 where β is the mode's propagation constant, and k=2π/λ.

$$b = \frac{(\beta/k)^2 - {n_2}^2}{{n_1}^2 - {n_2}^2} \approx \frac{(\beta/k) - n_2}{n_1 - n_2} \tag{1-7}$$

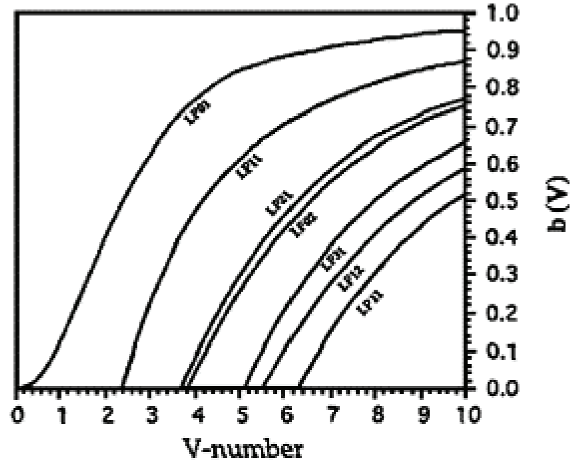

Figure 1-3: Plot of V-number vs. propagation constant for several common LP modes (courtesy of www,fiberoptics4sale.com)

Each curve in the figure represents the cut-off V-number for a mode or modes. The various modes are designated by LP notation, where and individual mode is referred to as LP_{lm} where the *l* and *m* subscripts refer to the number of radial and azimuthal zeros in the power distribution of the mode in the fiber. Figure 1-4 illustrates the power distribution for several modes. For a single mode fiber, only the LP_{01} mode will propagate, whereas for a multimode fiber the number of modes can be estimated using Figure 1-3 or Equation 1-6. Mode numbers are representative of the path traveled by a particular mode, where lower order modes will more closely approximate the axis of the fiber while higher order modes will travel a significantly longer distance (Figure 1-5).

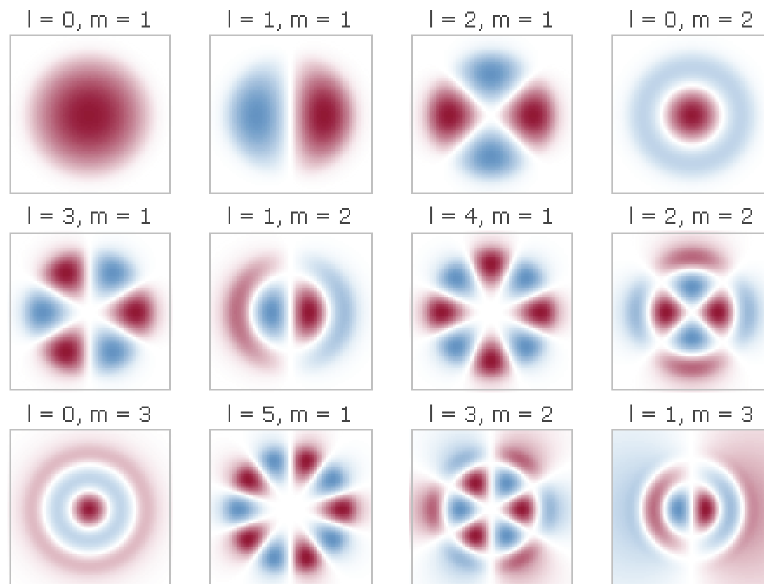

Figure 1-4: Optical power distribution of common LP modes (courtesy of www.fiberoptics4sale.com)

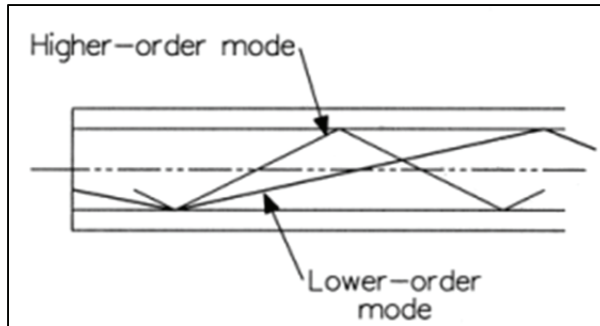

Figure 1-5: Ray trace diagram illustrating the difference in path length and internal reflection angle of higher and lower order modes (courtesy of www.fiberoptics4sale.com)

1.2 Temperature Sensing Methods

1.2.1 Mechanical Temperature Sensors

Mechanical thermometers are commonly used by the public for temperature sensing in everything from household appliances such as ovens and thermostats, to medical applications like the oral thermometer. The mechanism of operation for these temperature sensors (or thermometers) is generally driven by the thermal expansion most materials experience when subjected to heat. As the material comprising the sensing element is exposed to heat, a usually visible change will occur, which can be correlated with a specific temperature. Examples of this type of thermometer include bulb thermometers, in which a liquid in a sealed container expands predictably with temperature indicating temperature as it expands to fill the container, and bimetallic strip thermometers that utilize metals with dissimilar thermal expansions bonded together. In the case of bimetallic strips, the differential expansion leads to a displacement of the free tip of the thermometer which is then used to indicate the temperature. Mechanical thermometers are amongst the easiest type of temperature sensor to implement, however they also suffer the drawback of needing to be read at, or very near, the point of measurement, which can be difficult in some situations.

1.2.2 Electrical Temperature Sensors

Electrical temperature sensors, as the name implies, utilize electricity to transduce temperature. The advantage gained in this type of sensing is the ability to locate the sensing element remotely from the point at which the temperature is read. Thermocouples, thermistors, and resistance thermal detectors comprise some examples of this type of thermal.

Thermocouples operate by using the Seebeck effect (also known as the thermoelectric effect), in which conductors produce a voltage in the presence of a thermal gradient. Thermocouples have the advantages of being inexpensive, able to sense over a broad range, and being self-powered. Limitations of the thermocouple include the limited accuracy, which can often exhibit errors of greater than one degree Celsius, and susceptibility to both corrosion and electromagnetic interference (EMI).

Thermistors and resistance thermal detectors (RTD) utilize a resistance change in the sensing element to transduce temperature. Thermistors are generally composed of ceramics while RTD sensing elements are formed from pure metals. While thermistors and RTDs exhibit greater accuracy and precision than thermocouples, they are limited in sensing range, with thermistors generally operating below 130°C and RTDs below 1000°C (with most commercial applications being held below 700°C due to increasing errors occurring at higher temperatures due to contamination of the platinum element [7]), by the necessity of providing power to the sensing element, in addition to the environmental difficulties also encountered with thermocouples.

1.2.3 Optical Temperature Sensors

Optical temperature sensing utilizing fiber optics is a relatively new field and holds many draws as a remote temperature sensing technology. Of particular note are optical sensors' specific advantages over electronic temperature sensing including their immunity to EMI, the capability of extremely long distance remote sensing, and their relative insensitivity to corrosion. As mentioned in the abstract, several common methods of optical temperature transduction are in use today, including the pyrometer, Fiber Bragg Gratings, and interference based systems such as the Fabry-Perot Interferometer (FPI). Forms of optical thermometry that do not included guided light are beyond the scope of this work and will not be discussed.

The fiber optic pyrometer is generally used for very high temperature sensing. Utilizing fiber optics allows the pyrometer to be located remotely from the sensing electronics, and the advent of crystalline fibers for guiding IR light allowed for substantially increased operating temperatures of up to 2600°C [8]. The method of operation for the fiber optic pyrometer is to collect optical radiation from a target and channel that energy through the fiber optics to a photo-detector. Used in a non-contact mode of operation, the pyrometer can sense up to 4000°C with systems based on blackbody radiation detection [9]. Fiber optic pyrometers sense light intensity

and wavelength to transduce temperature at the target. Of the three types of optical thermometers discussed here, only the pyrometer is capable of non-local temperature detection. The wavelength of the peak intensity corresponds to a specific temperature, as illustrated by Figure 1-6.

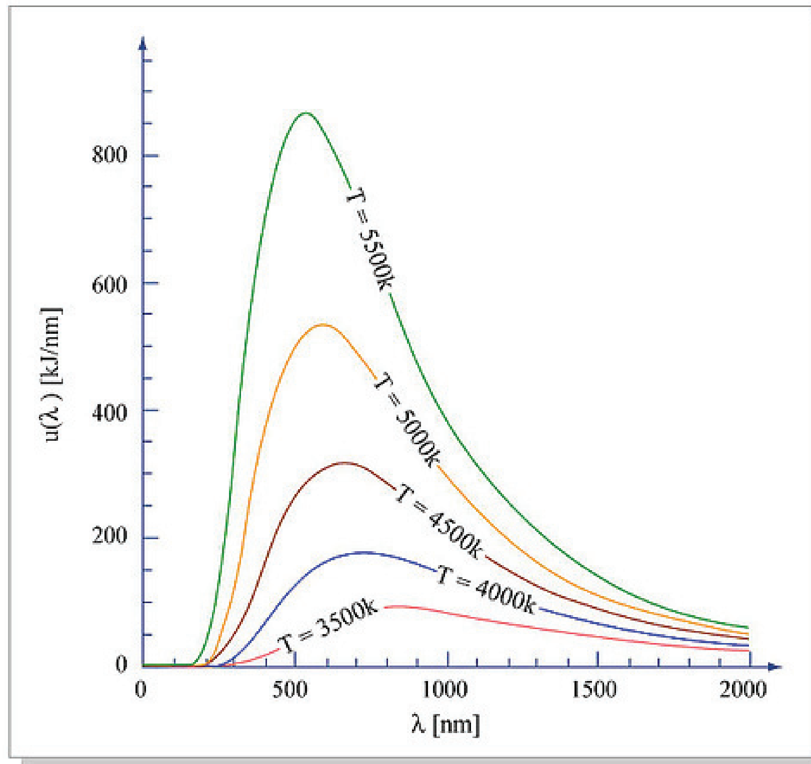

Figure 1-6:Blackbody spectral radiance of electromagnetic radiation at various temperatures (courtesy of MIT OpenCourseWare)

FBG based systems are a combination of mechanical and optical means to accomplish temperature transduction. The FBG is comprised of a periodic series of changes in the index of refraction in the core of the fiber. The period of the grating forms a dielectric mirror based on the principle of Fresnel reflection, which is specific to a certain wavelength of the optical spectrum. The reflected, or Bragg wavelength, λ_B, is determined by the grating period, Λ, the wavelength of light, λ, and the effective index of refraction, n_e. Equation 1-8 defines the relationship of the Bragg wavelength with grating period and effective index of refraction.

$$\lambda_B = 2n_e\Lambda \tag{1-8}$$

The effective index of refraction is a relationship between the wavelength and the mode's propagation constant, which quantifies the difference in phase delay of the light in the fiber relative to a vacuum. Equation 1-9 defines this relationship.

$$n_e = \beta \frac{\lambda}{2\pi} \tag{1-9}$$

Fiber Bragg Gratings can be produced in several different types and styles to achieve the desired reflection characteristics from the grating. Temperature transduction from an FBG is accomplished by the change in period of the grating induced by thermal expansion of the fiber core. The sensed factor in this method is the preferential reflection of a certain wavelength of light detected by a spectrometer.

Interferometry offers another method of temperature sensing with fiber optics. Of specific interest in this work is Fabry-Perot Interferometry (FPI) in which successive reflections of a light ray create an interference pattern that is modulated by the distance between the reflecting surfaces [10]. The modulation of the interference pattern as a result of thermally induced changes in the Fabry-Perot cavity provides the sensing factor for this type of thermometer. A more detailed discussion of Fabry-Perot Interferometry will be covered in Section 2.1.

1.3 High Temperature Optical Sensor Selection

The work performed for this thesis comprised a continuation of work on a high temperature, semi-distributed thermometer as funded by Pratt and Whitney for use in a limited space application. As such, the specifications for operation included a temperature maximum of 1600°C, a miniature sensor element, a minimized egress impact due to sensor installation, and resistance to corrosion and EMI. In response to these requirements, an interference based method was selected. Interferometry was chosen due to its applicability for use with sapphire optical components and expected range of temperature operation. The writing of FBG gratings in sapphire fiber is not a viable option at this time and FBG structures in silica fibers are known to bleach beyond use at temperatures of 1100°C [11]. The likely necessity for embedding the sensor within a structure deemed the pyrometer unsuitable for this application.

A sensing element comprised of optical sapphire components and alumina and zirconia framework structures was chosen as the materials of choice to satisfy temperature, corrosion resistance, and EMI insensitivity requirements. Sapphire optical materials offered the ready

availability of commercially produced fibers and wafers to form waveguides and Fabry-Perot etalons respectively.

1.4 Thesis Topic Organization

The coming chapters of this thesis will expand on the theory of sensor operation and physical creation of the sensor. In Chapter 2, the theory behind the transduction of temperature using Fabry-Perot Interferometry will be discussed, along with a discussion of the basic physical elements which make up the system. Chapter 3 will cover the interrogation method used to determine temperature from the sensor's raw signal as well as the criteria used to assess the quality of sensor components and overall sensor operation. Chapter 4 details the physical methods used in the creation of sensor components and the fabrication of a sensor element from these components. A means of chaining individual sensors into a semi-distributed sensing scheme is provided in Chapter 5, and Chapter 6 covers potential avenues to improve and continue the presented research as well as providing a summary of work completed.

Chapter 2: Sensing Method Principles

2.1 Fabry-Perot Interferometry

Fabry-Perot Interferometry involves the formation of wavelength dependent interference patterns as a result of phase mismatches in a beam of light travelling different distances following partial reflection from consecutive surfaces. Reflective surfaces can be formed either intrinsically or extrinsically; in the former case, the light does not leave the fiber before being reflected off of sequential reflectors whereas in and Extrinsic Fabry-Perot Interferometer the light leaves the fiber and is reflected off of a separate structure. A cavity to form the interferometer is comprised of two parallel reflecting surfaces spaced closely together. A cavity formed by a single solid material, with the front and rear faces creating the parallel reflecting surfaces, is termed a Fabry-Perot etalon.

The interference pattern generated by the Fabry-Perot interferometer is caused by alternating constructive and destructive interference of wavelengths of light in response to whether the reflected beams of the wavelength are in or out of phase (Figure 2-1).

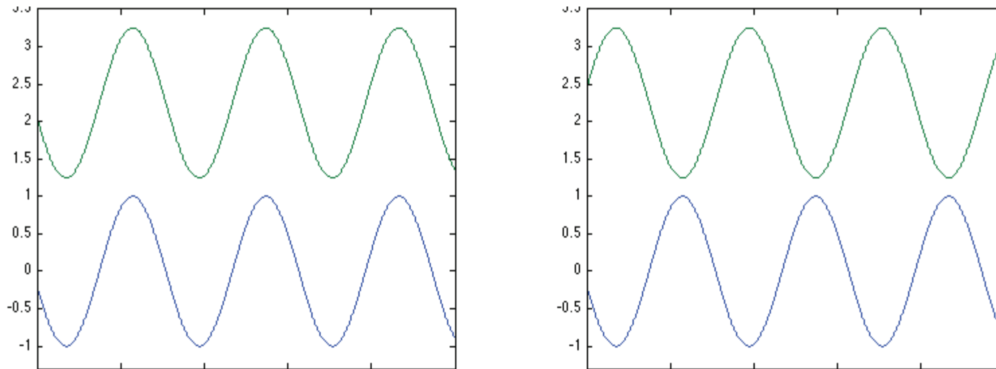

Figure 2-1: Examples of wavelengths that are in phase (left) versus wavelengths that are out of phase by Pi radians

Equation 2-1 defines the phase difference between each reflection as δ, where λ is the wavelength (in a vacuum), *n* is the index of refraction of the cavity, *l* is the distance between the reflecting surfaces, and *Θ* is the angle of incidence of the beam (Figure 2-2).

$$\delta = \left(\frac{2\pi}{\lambda}\right) 2nl \cos\theta \qquad (2\text{-}1)$$

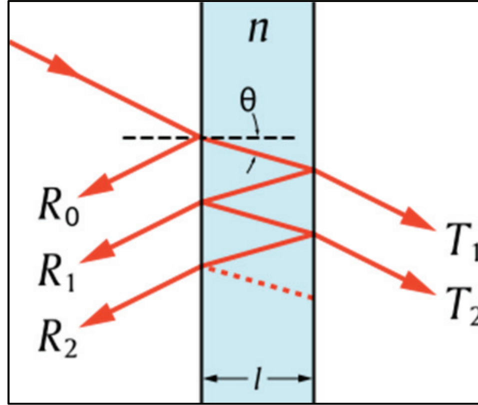

Figure 2-2: Diagram of a Fabry-Perot etalon where theta is the angle of incidence. Multiple internal reflections give rise to both transmitted and reflected rays (courtesy Stigmatella Aurantiaca via Wikimedia Commons)

The amount of constructive or destructive interference is given by the transmittance function, T_e, shown in Equation 2-2 (which assumes that the reflectance, R, of each reflecting surface is equal).

$$T_e = \frac{(1-R)^2}{1+R^2-2R\cos\delta} = \frac{1}{1+F\sin^2(\delta/2)} \tag{2-2}$$

Where F is the coefficient of finesse, given by Equation 2-3, and reflectance (or coefficient of reflection), R, is calculated using the Fresnel equations (Equation 2-4).

$$F = \frac{4R}{(1-R)^2} \tag{2-3}$$

$$R = \left|\frac{n_1\cos\theta_i - n_2\cos\theta_t}{n_1\cos\theta_i + n_2\cos\theta_t}\right|^2 \tag{2-4}$$

$$OPD = n(AB+BC) - n'(AD) = 2nl\cos\theta \tag{2-5}$$

In the theoretical case, complete transmittance of a beam through the cavity would occur when the optical path length difference (OPD), or the difference in lengths traveled by the beam's reflected and transmitted components, given by Equation 2-5 is an integer multiple of the wavelength (Figure 2-3).

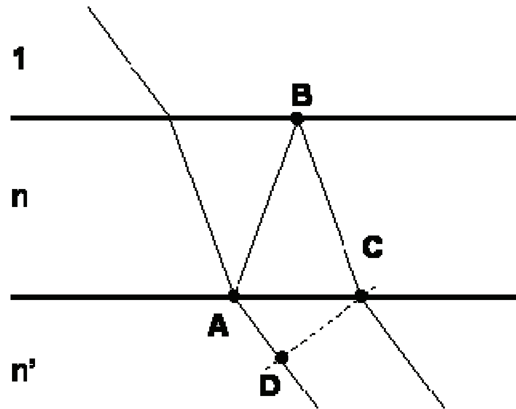

Figure 2-3: Sketch of the ray paths involved in the calculation of OPD between two consecutive transmitted rays (Courtesy Universitat de Barcelona)

In the complementary manner shown in a plot of Transmission/Reflection versus wavelength for two etalons with different coefficients of finesse (Figure 2-4), at transmittance minima, the reflected light will be maximized. The phase difference described by Equation 2-1 is periodic with a changing cavity length, *l*. By describing this periodicity in terms of radians we find that absolute constructive interference occurs at 0 and 2π resulting in the original amplitude being transmitted forward (in an ideal case). In complement to this, absolute destructive interference will occur at π, resulting in the transmission minima observed in Figure 2-XB. This periodic occurrence of maxima and minima are described by the complex exponential function. By squaring this function, we are able to convert the result to intensity by wavelength as shown in Equation 2-6 where φ_0 is the initial phase of the light beam.

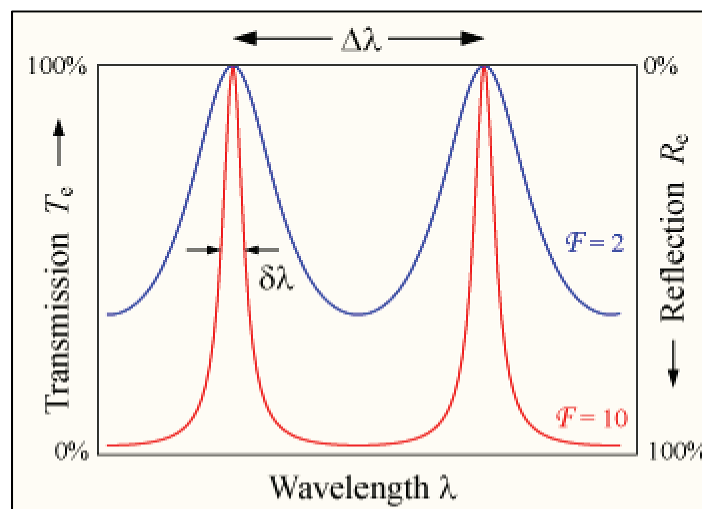

Figure 2-4: Plot of etalon optical power transmission/reflection by wavelength (courtesy WikimediaCommons)

$$I(\lambda) \propto \left| R_1 e^{-j\pi} + R_2 e^{-2j\pi\frac{2\pi OPD}{\lambda}} \right|^2 = {R_1}^2 + {R_2}^2 - 2R_1R_2\cos\left(\frac{2\pi OPD}{\lambda} + \varphi_0\right) \quad \text{(2-6)}$$

This change in intensity by wavelength forms the interference pattern of the Fabry-Perot interferometer. Following on this, it becomes apparent that a change in the cavity length will result in a change in the interference pattern generated by the interferometer. The apparent periodicity in the interference pattern is due to the cosine term in Equation 2-6 as shown in Equation 2-7, and it is this term that contains the modulation information with respect to the thickness of the Fabry-Perot cavity.

$$I(\lambda) \propto \cos\left(\frac{2\pi OPD}{\lambda}\right) \quad \text{(2-7)}$$

The utility of the Fabry-Perot interferometer as a thermometer element comes to play with the use of a broadband light source. In this case it is useful to look at the interference pattern in terms of light intensity by wavelength. Let us assume a uniform intensity over a range of wavelengths composing a broadband light source injected into a Fabry-Perot interferometer and a spectrometer positioned to receive the transmitted light beyond the interferometer. As we move across the spectrum of wavelengths sensed by the spectrometer, the relative intensity will vary with the wavelength. This fact is driven by the change in phase induced by the additional length travelled by the partial beam of light reflected in the interferometer.

As stated in section 2.1, complete transmittance (and, accordingly, complete reflectance) will occur when the OPD is an integer multiple of a wavelength (Equation 2-8, where m is any positive integer).

$$OPD = m\lambda \quad \text{(2-8)}$$

Examination of this relationship between OPD and wavelength, along with Equation 2-2, indicates that the phase difference will decrease with wavelength, and accordingly the intensity maxima discussed above will decrease in frequency as the wavelength increases. Figure 2-5 illustrates the change in phase by wavelength for a cavity of arbitrary length by plotting the cosine of δ vs. wavelength.

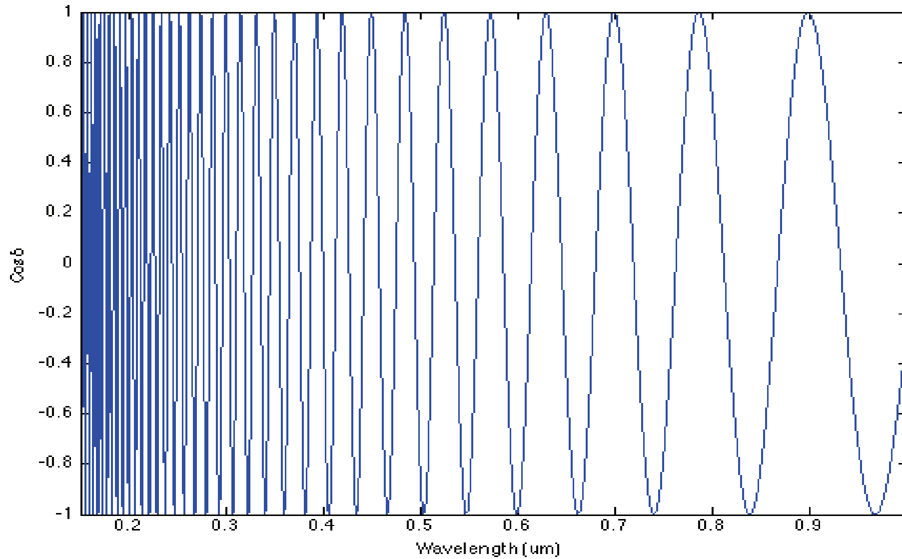

Figure 2-5: Plot of cosine of phase delay experienced by a ray reflected by a Fabry-Perot cavity of arbitrary length versus wavelength

2.2 Basic System Setup

The basic components required to form and interrogate a thermometer from the Fabry-Perot interferometer discussed above include an interferometry cavity to provide a sensing element, a means of delivering light to the sensing element in the form of the connecting optical fibers, a light source, and a spectrometer. Figure 2-6 shows an overview of the system set-up showing these relevant components. The following sections will go into greater detail for each of the individual components.

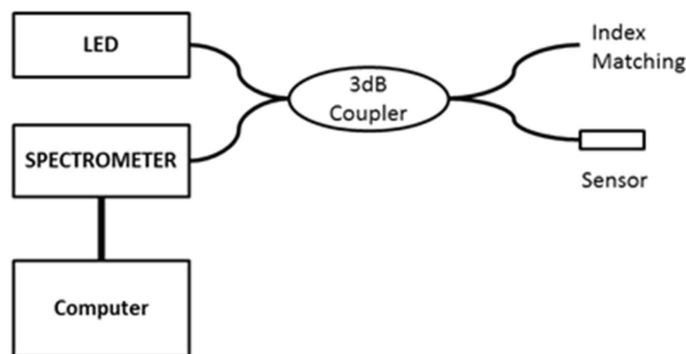

Figure 2-6: Schematic diagram illustrating the major components of the Fabry-Perot optical thermometer system set up for this project

2.2.1 Sensing Element

The basic sensing element used during a majority of the project work consisted of a Fabry-Perot etalon composed of a thin sapphire wafer. In order to maximize the light intensity reflected back into the system, the orientation of the wafer must be as close as possible to perpendicular to the axis of the lead in fiber. The supporting structure of an alumina or zirconia ferrule is used to accomplish this alignment (Figure 2- cartoon of fiber wafer alignment w/ferrule) and mitigate loss of higher order modes. Alternate means of accomplishing etalon and fiber alignment will be covered in Chapter 4. The parallelism and surface quality of the sapphire wafer is of great importance to the operation of the sensor [12], and great pains were taken to ensure the best possible etalon fabrication, as will be covered in Section 4.1.

2.2.2 Light Injection System

Use of a fiber coupled light emitting diode (LED) to provide illumination allows for abundant optical power to be delivered to the sensing element. LEDs also provide a much wider bandwidth than a laser light source for significantly less expense. The LED used for this project exhibit a central wavelength of 850 nm with a full width at half maximum (FWHM) bandwidth of approximately 50 nm. The light from the LED is coupled into 100/140 (100 micron diameter core, 140 micron diameter cladding) silica multi-mode fiber (MMF) and passed through a 2x2 3-decibel (dB) coupler, which splits the light equally into the two exit fibers. One of these fibers terminates in an anti-reflective end created with index matching materials, an attenuation coil, or both, and is of no more consequence to the system. The second fiber extends the light injection system to the sensor head via the silica MMF. At a certain distance from the sensor head, the silica fiber is spliced to a 75 micron single crystal sapphire fiber. This allows light to be guided to the sensor head in high temperature environments without the attenuation associated with dopant migration in silica fibers at high temperatures. The splice point between the silica and sapphire fibers is performed with a Fujikura FSM-30P Arc Fusion Splicer. Using the splicer, the two fibers are aligned axis to axis. As the sapphire fiber is smaller than the 100/140 silica fiber, the splicing process allows the sapphire fiber to mate with the core of the silica fiber. To accomplish this without fracturing the silica fiber or causing the sapphire fiber to become amorphized a low arc power and duration are prescribed. Previous experience in the Center for

Photonics Technology (CPT) laboratory provided the guidelines for splicing settings with an arc duration of .025 seconds and an arc power of 20/64.

Sapphire fiber is highly multimode and will excite additional modes from the light passed to it from the silica MMF. This difference in modal volume becomes important on the return trip of light reflected from the sensor element as the reflectance of the sapphire wafer which forms the Fabry-Perot etalon is 0.076, meaning that at each surface only 7.6% of the incident light will be reflected back to the spectrometer for detection. At the interface between the sapphire and silica fiber the additional higher order modes excited in the sapphire fiber will not be collected by the owing to the mismatch in numerical apertures between the two fibers. This mismatch will further contribute to attenuation of the light reflected back to the spectrometer, and by extension, the signal obtained from the sensing element.

The light reflected from the sensor element will propagate from the sapphire fiber through the silica fiber to the 3 dB coupler at which point the light will again be split between two fibers, one returning to the LED ineffectually, and the other arriving at the spectrometer. In an ideal case, neglecting intrinsic attenuation of the fibers, numerical aperture mismatches, and splicing losses, the optical intensity from the LED will undergo a 50% reduction due to the first encounter with the coupler, a 93% reduction of the remaining intensity at the first face of the etalon (returning 3.5% of the initial intensity) and again at the second face (which returns 3.255% of the initial intensity), and another 50% drop of this light on the second trip through the coupler resulting in only 3.38% of the initial injected light being available at the spectrometer. It is apparent that in the best of conditions, the signal received from the sensor element will be very weak. To mitigate a decrease in signal-to-noise ratio (SNR), splicing points must be created with precision, and all optical surfaces and structures fabricated to as high a quality as possible.

2.2.3 Spectrometer Options

The choice of spectrometer for the system was driven by the signal expected from the sensing element in conjunction with expense and system complexity. Available in the CPT laboratory were Micron Optics swept laser wavelength measurement systems (CTS), ANDO optical spectrum analyzers (OSA), and Ocean Optics solid state USB spectrometers (OOI). The Micron Optics CTS offered a turnkey solution by combining the spectrometer and light source in a single package; however the wavelength range covered by the instrument was too limited for the

expected fringe spacing of the sensor etalon. The ANDO OSA provided the wavelength range necessary for the sensor interrogation, but integration into a portable system was hindered by the size of the instrument, and the scanning rate was considered to be too slow for the project's needs. The Ocean Optics spectrometers offered a small footprint solution with a simple interface to a computer based signal processing system. The Ocean Optics spectrometer became the component of choice along with the LED light source.

2.3 Basic System Signal Processing

In Section 2.2.2 an expected intensity was described for an ideal case, however, aside from the expected losses that are not included, there are additional sources of light intensity in the system that will be returned to the spectrometer which will act to weaken the sensor's SNR. Reflections in the system are a main source of additional light received by the spectrometer. Of particular note are the reflections caused by splices, including silica-to-silica fiber splices and the more prominent silica-to-sapphire splice and the reflection from the end of the sapphire fiber, which has the same reflectance as the surfaces of the sapphire wafer etalon. Blackbody radiation from system components in the hot zone and the dark current of the photo-detector will also contribute to the overall intensity of light reported by the spectrometer. Equation 2-9 [13] combines these effects to form a more complete picture of the intensity by wavelength reported from the Ocean Optics spectrometer.

$$I_{tot}(\lambda) = I_B(\lambda) + I_D(\lambda) + I_{source}(\lambda)\left[r_{splice} + r_{end} + r_{A1} + r_{A2} - 2V\sqrt{r_{A1}r_{A2}}\cos\left(\frac{2\pi \times OPD}{\lambda} + \varphi\right)\right] \qquad \textit{(2-9)}$$

where I_{tot} is the total intensity reported by the spectrometer, I_B is the contribution due to blackbody radiation, I_D is the contribution from the spectrometer's dark current, I_{source} is the original intensity produced by the light source, r_{splice} and r_{end} are the sapphire/silica splice and sapphire fiber end reflections respectively, and r_{A1} is r_{A2} is are the reflections from the front and rear faces of the sapphire etalon. The total intensity does not include light from the reflections that is lost due to coupling losses and fiber attenuation. The interference pattern generated by the sensor head etalon will be propagated back to the spectrometer and the intensity map used to determine the OPD encountered by the reflected light. The processing of the signal from the sensor head is performed using MATLAB and results in the calculated OPD of the cavity. From equation 2-4, it is evident that using the calculated OPD along with the coefficient of thermal

expansion (CTE) of the sapphire wafer we can determine the theoretical cavity thickness, and subsequent OPD, for any temperature; however, variations in the sensor's response to thermal expansion due to fabrication issues or material defects might cause a deviation from theoretical values. A deviation from the theoretical calculation would result in the reporting of an incorrect temperature at the sensor head. To mitigate this, calibration data created from the sensor head's response at various temperatures can be obtained through experimental means, and the equation of a curve fitted to the experimental data used to determine the temperature from the calculated cavity OPD.

Chapter 3: Sensor Interrogation and Evaluation

3.1 Determination of Cavity Distance

From Equation 2-7 we know that the intensity, as modulated by the sensor head interferometer, is proportional to the cosine term of Equation 2-6. In kind, the cosine term of Equation 2-8 is the only quickly varying portion of the equation with respect to changing temperature at the sensor head, and is the only point at which the OPD occurs. We thus need only the OPD to demodulate the temperature at the sensor head. The most straightforward way to accomplish this would be by creating a system of equations using the wavelengths of the maxima created in the interference pattern. By manipulating Equation 2-6 we can arrive at the realization that the consecutive maxima will correspond to consecutive integer values of *m*, as demonstrated by Equations 3-1.

$$\frac{OPD}{\lambda_1} = m \quad , \quad \frac{OPD}{\lambda_2} = m + 1 \tag{3-1}$$

Subtracting these equations yields

$$\frac{OPD}{\lambda_2} - \frac{OPD}{\lambda_1} = 1 \tag{3-2}$$

This leads us to the calculation of the OPD from the wavelengths of two peaks as shown in Equation 3-3.

$$OPD = \frac{\lambda_1 \lambda_2}{\lambda_1 - \lambda_2} \tag{3-3}$$

While this method is useful to quickly estimate the OPD of the etalon, noise in the signal can create significant changes in that estimate. Additionally, the spurious reflections in the system can form unintentional Fabry-Perot interferometer cavities, which will be overlain on the intended signal causing difficulty in determining adjacent peaks. These difficulties indicate that a more sophisticated demodulation scheme is required. Shen and Wang published work in 2005 on using a frequency-estimation based algorithm [14] to determine cavity distance. As briefly discussed in Section 2.1, the phase change and therefore peak intensity positions are not linear with wavelength, but rather, as inspection of Equation 2-1 reveals, with one over the wavelength.

This value is also known as the wave number. By taking the fast Fourier transform (FFT) of the interference pattern generated by the sensor cavity with respect to the wave number rather than the wavelength, the fringes generated will occur with a regular sinusoidal periodicity as described by Equation 3-4.

$$(\lambda) = I_B\left(\frac{1}{k}\right) + I_D\left(\frac{1}{k}\right) + I_{source}\left(\frac{1}{k}\right)\left[r_{splice} + r_{end} + r_{A1} + r_{A2} - 2V\sqrt{r_{A1}r_{A2}}\cos(2\pi \times OPD \times k)\right] \quad (3\text{-}4)$$

As before, the only term which will be quickly varying is the cosine term, cos(2πOPD*k), and is therefore the only portion of interest. The frequency of the cosine term will be an obvious peak in the FFT, as shown in Figure 3-1, which will correspond to the OPD of the cavity.

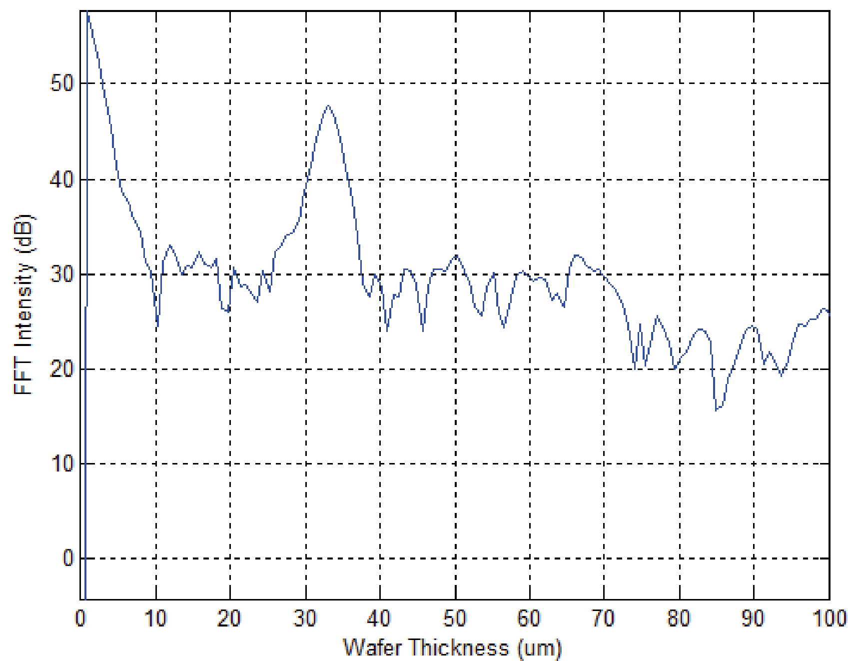

Figure 3-1: Plot of the Fourier transform of an interference pattern obtained from a sapphire wafer showing the signal peak corresponding to the wafer cavity sensed

This method also handles the spurious reflection based cavities encountered earlier as these cavities will be shifted to different frequencies from the intended cavity. One point where this frequency shift can still create problems lies in the sensor head design. By using an extrinsic Fabry-Perot interferometer (EFPI), there is necessarily an end of fiber reflection. By virtue of the sensor head design, this reflection is in close proximity to the first face of the sensor etalon, thus creating an interference cavity with a length very close to that of the intended sensor cavity. This geometry manifests itself in the demodulation of the sensor's signal as a double peak at the frequency of the sensor element. In such cases, assuming the second peak is distinct, the

intended signal should always be the lower frequency peak, as the gap between the fiber end face and the back reflection of the etalon, which created the peak, will always be longer than the thickness of the etalon alone.

3.2 Sensing Element Quality

The ability to sense temperature using the EFPI sensor head described earlier is dependent on the quality of the intensity modulation signal that reaches the spectrometer. As discussed in Section 2.2.2, the reflected intensity from the EFPI is significantly lower than the source light. Because of this, it is important to maximize the modulation created by the sensor element to prevent swamping of the signal from potential noise sources. In the ideal case, the EFPI etalon will exhibit perfect interference of all light beams encountering the etalon and the intensity received by the spectrometer would be a perfect representation of the interference pattern. However, imperfections in the system such as losses in the fiber, spurious reflections and noise (such as blackbody radiation) discussed previously, and etalon quality and alignment will also contribute to the signal received by the spectrometer. Each of these factors serves to degrade the signal by either contributing or reducing intensity. Of these factors, only the etalon quality and alignment, and to a lesser amount, splice point reflections, can be handled through fabrication quality control. Before discussing the process of etalon quality it is useful to understand the characteristics of the expected signal and how to evaluate its quality.

3.2.1 Fringe Visibility

The reflected intensity, which has been modulated by the etalon, forms an interference pattern based upon the source light injected into the system. Let us assume that the injected intensity from the LED has a Gaussian distribution over the wavelengths emitted, as shown dashed on Figure 3-2. Were the intensity reflected by the etalon perfect (in this case with a surface finesse of 10, which is significantly higher than that of sapphire), the interference pattern would be given by the solid line. The dash-dot line represents the reflected intensity of an un-modulated reflection. The difference between the maximum value of the interference pattern and the maximum value of the DC component of the signal represents the fringe visibility of the interference pattern, which is unity in this ideal case. As might be expected, the experimental

results are not ideal and the fringe visibility (FV) is reduced by the noise sources previously enumerated.

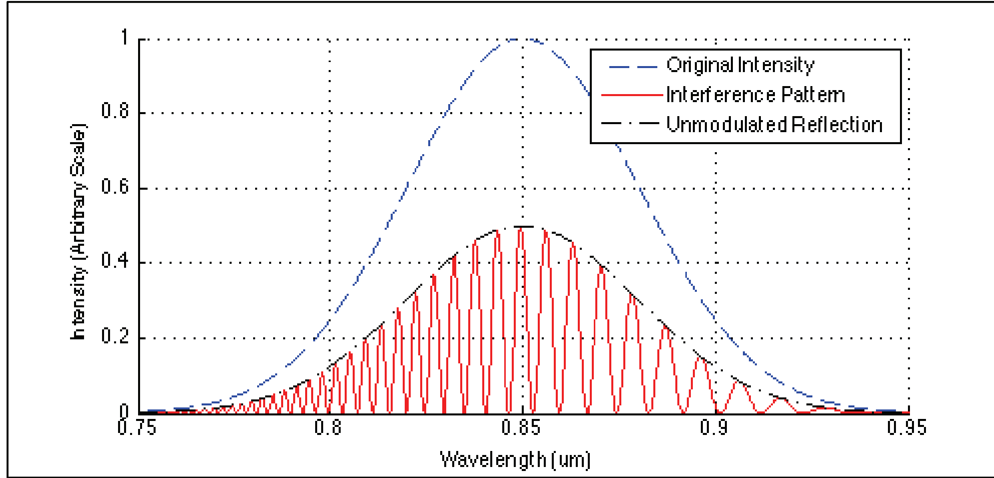

Figure 3-2: Plot of an ideal interference pattern for an interferometer which experiences no losses and no noise. Transmission maxima are represented by the zero intensity points

Figure 3-3 illustrates the interference pattern of a typical sapphire etalon. Sapphire wafer etalons comprise a low-finesse [15] surface (Equation 3-6) due to the low reflectivity of a sapphire-air interface, which is calculated in Equation 3-5 to be approximately 7.6% using Equation 2-4 assuming a normal beam incidence ($\Theta = 0°$) and an index of refraction of sapphire = 1.76.

$$R = \left|\frac{1\cos 0 - 1.76\cos 0}{1\cos 0 + 1.76\cos 0}\right|^2 = 0.0758 \tag{3-5}$$

$$F = \frac{4 \times 0.0758}{(1 - 0.0758)^2} = 0.355 \tag{3-6}$$

Due to this low reflectance, the received signal from the sensor head is very susceptible to being overwhelmed by DC noise components such as the end reflections and splice point reflections. As is seen in Figure 3-3, the fringe visibility is significantly less than ideal. To quantify the fringe visibility we can use Equation 3-7 [16] where I_{max} and I_{min} are the maximum and minimum intensity values, by wavelength, of fitted curves along the crest and troughs of the interference pattern respectively.

$$FV = \frac{I_{max} - I_{min}}{I_{max} + I_{min}} \tag{3-7}$$

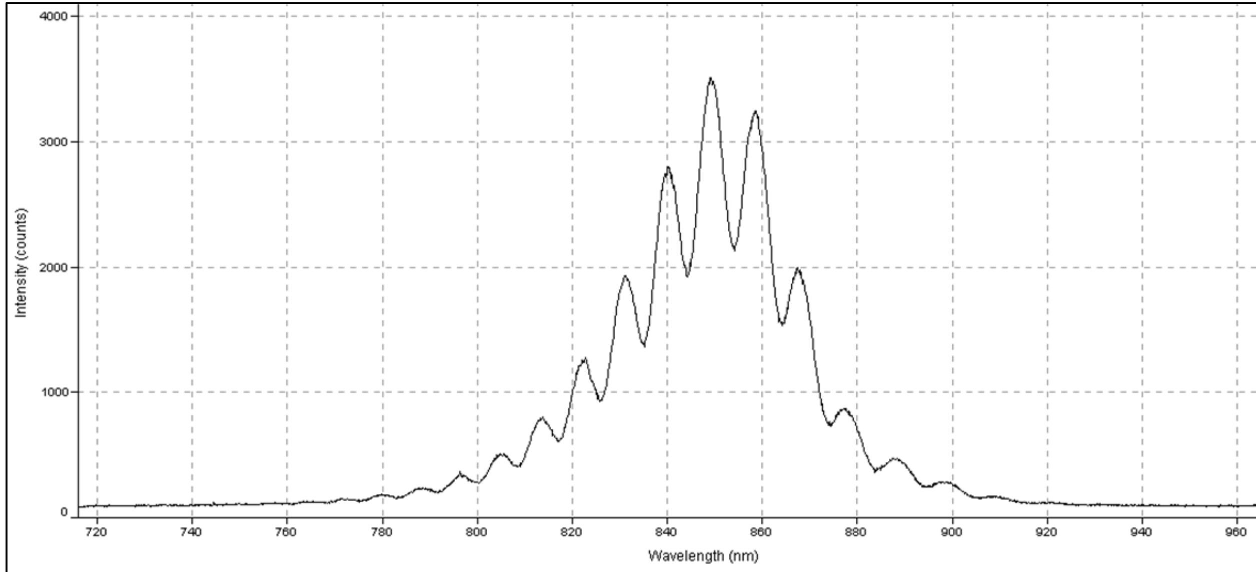

Figure 3-3: Interference pattern generated by a sapphire wafer interrogated with a fiber. Noise and spurious reflections combine with the signal to degrade fringe visibility

As specified in Section 2.2.2, the illumination source used in the system has a central wavelength of 850 nm, and it is at this wavelength that the greatest intensity is found, and therefore the wavelength at which the fringe visibility is most easily seen. As we can see from Equation 3-7, the ideal case (illustrated by Figure 3-2) would lead to a FV of 1, where as a FV of zero would indicate a complete degradation of the signal. The additional reflection from the sapphire fiber end will also contribute a 7.6% intensity gain to the output signal, and similarly, the silica sapphire splice, which has a lower reflectance of approximately 0.44% [17] will add un-modulated intensity. As the temperature in the sensing region increases, blackbody radiation will be coupled into the fiber, also adding to the un-modulated intensity. Each of these sources contributes to the $I_{\min}$ curve seen in Figure 3-4. Another source of FV degradation is caused by propagation losses in the sapphire fiber. Sapphire fiber exhibits an average loss of approximately 2 dB/m [18], meaning that long runs of sapphire fiber will significantly decrease the modulated signal with respect to splice point reflections in the fiber between the sapphire and the spectrometer. This decrease serves to reduce the modulated signal amplitude, reducing $I_{\max}$ with respect to $I_{\min}$, making the DC contributions from unwanted reflections more significant to the overall intensity received by the spectrometer and reducing FV.

3.2.2 Etalon Quality Control

While efforts are being made to evaluate methods of minimizing the contributions of unwanted reflections (such as using angled polishing of the sapphire at the sapphire-silica splice point [17]), it is clear that there is little than can be done to mitigate these intrinsic noise sources. Because of this, the quality of the EFPI etalon becomes of paramount importance, as it is a point in the sensor fabrication that can be controlled to a high degree. As mentioned in Section 2.2.1, wafer parallelism and surface quality are the driving factors behind a suitable etalon. Work completed by Ivanov in 2011 [17] sought to refine the polishing of commercially available wafers while also establishing and maintaining a high degree of parallelism between the reflecting surfaces of the etalon. Figure 2-2 (figure of etalon beams) indicates the means by which a beam of light reflected within the etalon travels a further distance and creates a phase mismatch with the initial (and subsequent reflected) beams. Figure 3-4 illustrates a situation where the etalon's surfaces are not parallel. In this case, the OPD of each subsequent reflection will be longer than the previous. The effect of this wedge angle, Ψ, is a smearing of the interference pattern, as the longer OPDs will create shifted minima and maxima in the interference pattern reducing overall FV. In the extreme case of a large enough wedge angle, the smearing of the interference pattern will approach a zero sum result and no interference pattern will be discernible. In the same manner, undulations in the active region (the portion of the wafer illuminated by the lead in fiber) of the sapphire wafer etalon will degrade FV.

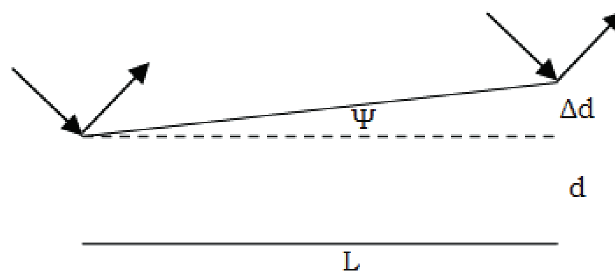

Figure 3-4: A schematic diagram of non-parallel etalon surfaces where the effect of delta-d acts to increase the path length experienced by the right hand ray as compared to the left hand ray when reflected between the two surfaces [18]

Experimental work completed at the CPT indicate that a planar wedge angle of less than 0.5° should be maintained to ensure a viable interference pattern (Figure 3-5).

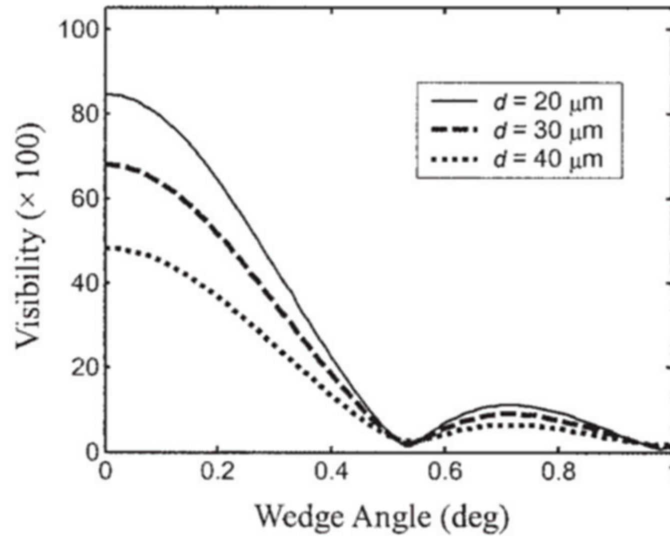

Figure 3-5: Plot of fringe visibility as a function of wedge angle between the Fabry-Perot etalon's reflective surfaces [13]

Evaluation of wafer parallelism was conducted using the Newton Rings method by which the wafer is illuminated by a coherent light source (for this work a 650 nm laser was used) and the interference pattern generated was visually inspected. Figure 3-6 illustrates the results of using the Newton Rings method of interferometry to determine wafer thickness. Each successive "ring" or band of interference indicates a difference in wafer thickness of one wavelength (650 nm). By counting the number of rings and measuring the distance covered by these rings, an estimation of wedge angle can be obtained using trigonometry. In practice, a qualitative analysis of the wafer ring patterns was used to select wafers for use as etalons, as well as selecting specific areas of the wafer to serve as active regions.

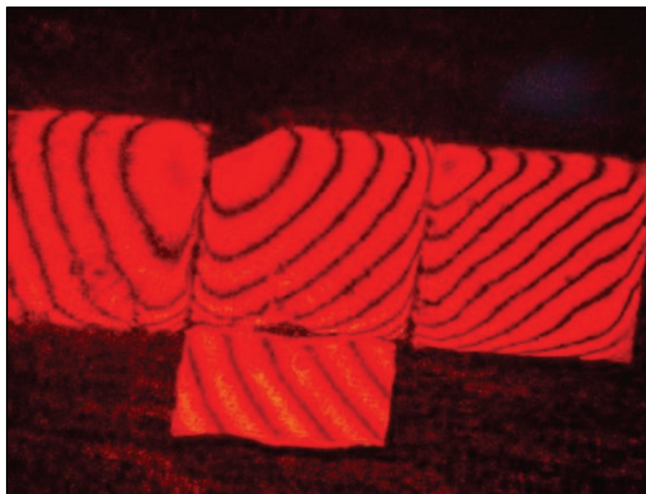

Figure 3-6: Newton Rings formed by the differential thickness of the sapphire wafer modulating the interference pattern of a 650 nm illuminating laser

Surface quality of the etalon refers to the mean roughness of the reflecting surfaces. Reflection from a surface can be either specular or diffuse (Figures 3-7) depending on the mean surface roughness and the wavelength of light encountering that surface. For specular reflection to occur, the mean surface roughness must be substantially smaller than the wavelength of light encountering the surface. In terms of the system described in Section 2.2, this means that the mean surface roughness must be significantly less than 850 nm to ensure that undue scattering does not occur at the surfaces of the etalon. To accomplish this, sapphire wafers were polished under a platen designed to maintain parallelism between the upper and lower surfaces of the wafer with successively finer grits of diamond polishing paper (Figure 3-8). The final polishing grit of 0.1 μm was used to achieve a surface roughness of less than 100 nm to ensure specular reflection. Evaluation of the surface quality of wafers (fiber end faces were also examined for surface quality following polishing) was conducted using a high power microscope and a qualitative analysis of the surface for the presence of scratches.

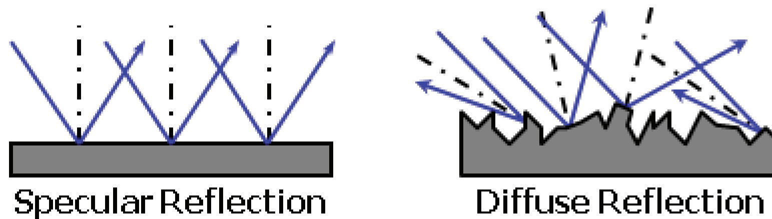

Figure 3-7: Diagrams of specular and diffuse reflection ray traces resulting from incident light impinging on two surfaces of different roughness

Figure 3-8: Hand polishing sapphire wafers was accomplished using a polishing plated to maintain wafer parallelism on a polishing wheel [18]

3.2.3 Etalon Length

A third factor in determining fringe visibility stems from the etalon's dimensions rather than the quality of the sapphire wafer. Work done by M. Han et al in 2004 [12] provided data for the relationship between fringe visibility and EFPI cavity length. As can be seen in Figure 3-9, a plot of the data indicates that a shorter gap length increases the fringe visibility. Unfortunately, the thinner the wafer, the more fragile it becomes and a tradeoff must be made between FV and the ability to handle to wafer for sensor fabrication. In practice, wafers thinned to as little as 10 microns were created, but the losses incurred in fabrication and difficulty in handling outweighed the gains in FV, therefore the practical lower limit for wafer thinning hovered around 20 microns.

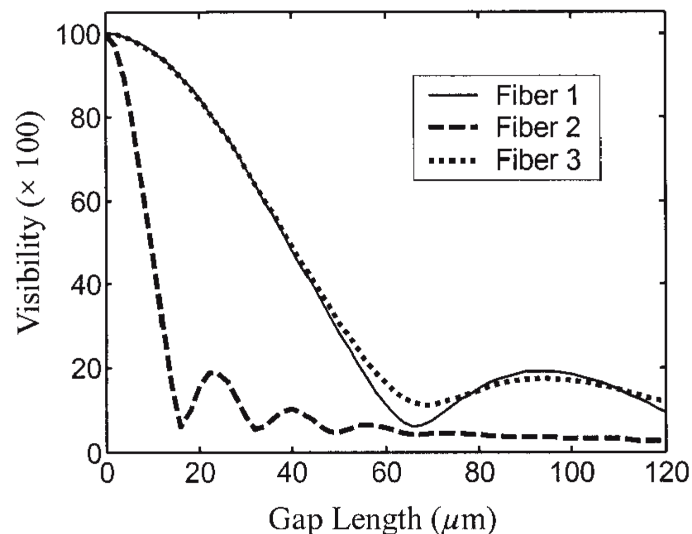

Figure 3-9: Plot of fringe visibility as a function of gap length [13]

Along with the physical difficulties associated with extremely thin wafer etalons, the system light source places additional constraints on etalon length. As noted in Section 2.2.2, the light source selected for this project has a full range of wavelengths of only 200 nm. Any interference pattern generated by the etalon must necessarily fall within the range of wavelengths provided by the light source. The signal processing described in Section 3.1 requires several periods of the interference pattern to accurately determine the frequency and calculate the OPD. With this in mind, Equation 3- provides a means of estimating of the number of fringes in a given range of wavelengths.

$$N_{fringe} = \frac{2\Delta L}{{\lambda_c}^2} \times \Delta\lambda \quad (3\text{-}8)$$

Where N is the number of visible fringes, ΔL is the cavity length of the etalon, Δλ is the wavelength range, and λ_c is the central wavelength. Figure 3-10 shows a plot of N as a function of ΔL. As is apparent, at shorter cavity lengths the number of visible fringes decreases, which in turn would make demodulating the interference signal less accurate as fewer periods would be available to determine the interference pattern frequency. This result adds weight to the decision to place a lower limit on the etalon cavity length.

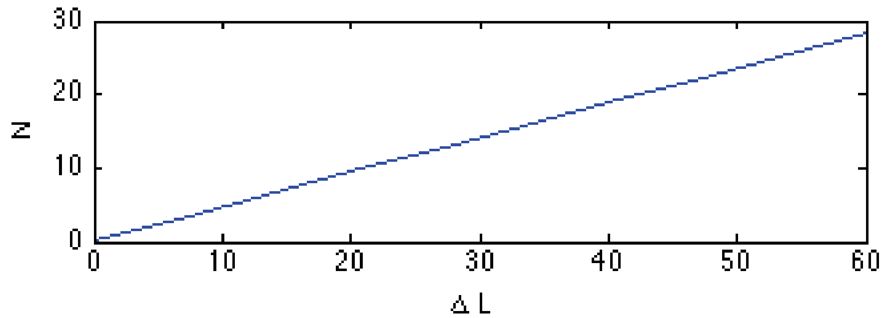

Figure 3-10: Plot of the number of fringes visible in a 200 nm bandwidth as a function of cavity length

Chapter 4: Fabrication of Sensing Elements

4.1 Wafer Etalon Design

4.1.1 Slot and End Sensor Designs

As briefly described in Section 2.2.1, the sensing element of the thermometer is composed of a thin sapphire wafer that acts as the etalon in an extrinsic Fabry-Perot interferometer. This wafer is aligned with a 75 μm diameter sapphire lead in fiber by means of a ferrule which also provides support to the wafer. Two sensor geometries were created to investigate the effects of wafer positioning in an embedded application as well as to provide a means for multiplexing several sensors with an inline configuration. The first geometry is an end sensor design, which places the wafer etalon at the end of the ferrule, maximizes the exposure of the active region of the wafer to the sensed environment to provide a rapid response time and easier fabrication process. The second geometry, a slot sensor design, places the wafer etalon into a slot cut into the ferrule providing greater support of the wafer and allowing for the alignment of a second fiber to provide a light guide to additional etalons. Figure 4-1 illustrates the two geometries with a cut-away diagram.

The design of the end sensor utilizes a 1 mm outer diameter (OD) alumina ferrule with an inner diameter (ID) of 250 microns to confine the sapphire fiber and align it with the wafer. The oversized ID eases the insertion and allows the fiber to be positioned to obtain the best fringe visibility from the wafer. The sapphire wafer is positioned on the end of the ferrule such that the most favorable location on the wafer is placed over the ferrule hole to be used as the active region and affixed in position with a ceramic adhesive (Cotronics 989F). After the adhesive fixing the wafer has cured, the sapphire fiber is inserted into the ferrule and manipulated to obtain the best possible FV. Once the position is determined, the fiber is carefully fixed in place with the ceramic adhesive. The alumina ferrule and adhesive were selected to minimize the differences in the coefficient of thermal expansion (CTE) between the sapphire components and the supporting structures. Table 4-1 provides a comparison of the CTEs of the various components of both sensor head designs.

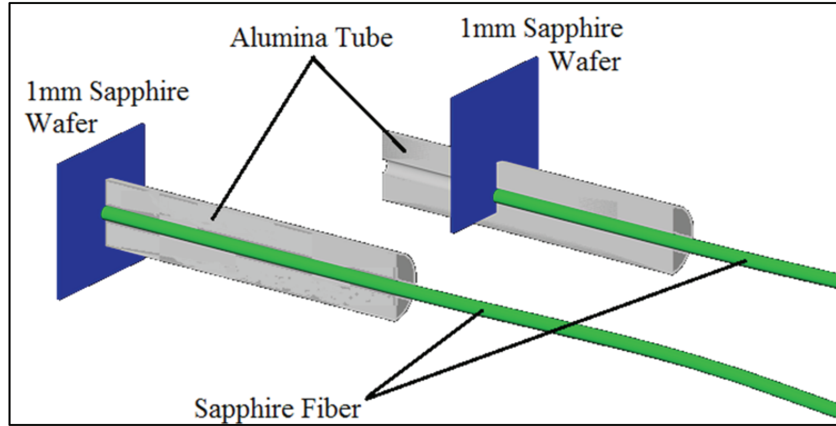

Figure 4-1: Cutaway representation of the end sensor (left) and slot sensor (right) designs utilized for Extrinsic Fabry-Perot Interferometric temperature sensing

The slot sensor design necessitated a greater confinement of the sapphire fiber to ensure propagation to additional inline fibers. To accomplish this, the alumina ferrule was replaced with a 1 mm OD zirconia ferrule that allowed for a smaller inner diameter of 80 microns. The ID of the zirconia ferrule was selected to allow for the margin of error in fiber diameter during the growth of the sapphire crystal while still being tight enough to ensure a perpendicular alignment with the wafer etalon and axial alignment with subsequent fibers, as well as being a stock size available commercially. To maximize fringe visibility in the slot sensor design, the wafer must be manipulated in the slot along with the fiber to arrive at the best possible active region. The depth of the slot and size of the wafer limit the range of positioning possible for this adjustment and require a wafer with a quality surface near an edge. As with the end sensor, both the fiber and the wafer are fixed in place with ceramic adhesive following alignment. In both designs the lead in sapphire fiber was approximately 15 cm in length. The lead in fiber length would become a function of the installation as the shortest length of sapphire is desired to reduce both cost and optical losses, but is driven by the position of the sensor in the heated zone and the length required to exit the heated zone to a point where the temperature would not exceed the capabilities of silica fiber.

Material	Coefficient of thermal expansion (CTE)
Sapphire (C-axis parallel)	5.90×10^{6}/°C (@ 70°C) to 9.77×10^{6} (@ 600°C)
Zirconia	10×10^{6}/°C
Alumina	8.4×10^{6}/°C
Cotronics 989F adhesive	8.1×10^{6}/°C

Table 4-1: A comparison of the coefficients of thermal expansion for the materials used to construct the sensor elements

4.1.2 Strain Cross Sensitivity Testing

A secondary objective of the project arose from the concerns of Pratt and Whitney over the potential for strain induced error to diminish the ability of the sensor head to accurately modulate temperature. While strain decoupled optical thermometers have been demonstrated previously [19] the system relied upon a compensation sensor to provide a means of eliminating the cross-sensitivity. The wafer etalon design previously described seeks to provide temperature sensing without strain cross-sensitivity and without compensation. To address this concern, strain testing was performed on both sensor designs to determine the extent of cross-sensitivity between the sensors' strain and thermal expansion responses.

To evaluate the EFPI sensors' cross sensitivity with strain, a laboratory test setup was constructed to facilitate strain transfer to both types of EFPI sensor geometries. An end sensor and a slot sensor were adhered to a stainless steel strain test plate measuring 50mm x 30mm x 2.2mm using ceramic adhesive. An Omega precision strain gauge was also adhered to the test plate between the two EFPI sensors (Figure 4-2) to monitor the strain applied to the plate. The two EFPI sensors and strain gauge were then embedded in the ceramic adhesive to a depth of ~0.5mm and allowed to air cure.

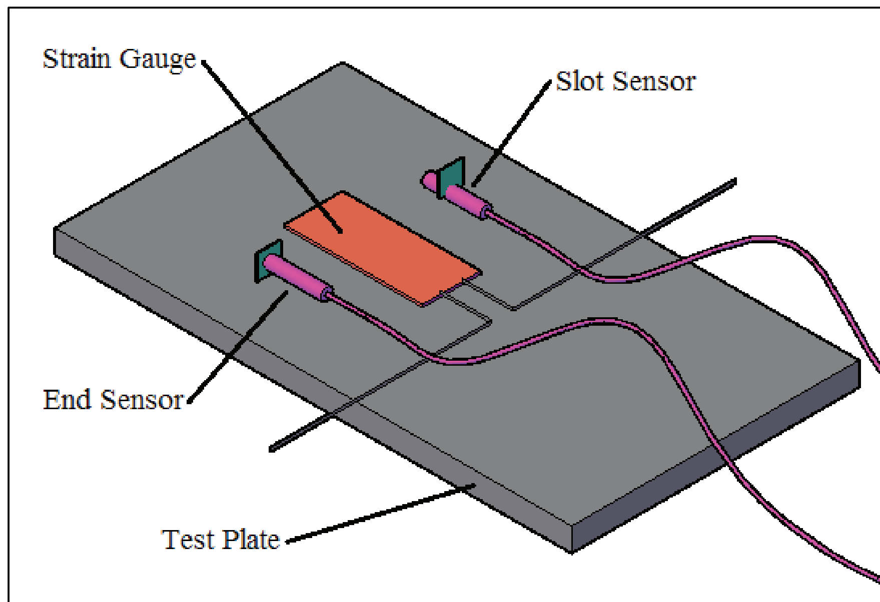

Figure 4-2: Strain cross-sensitivity testing plate sensor schematic indicating locations of two fiber sensors and foil strain gauge

The strain test plate with embedded sensors was then attached to a precision micrometer 3-axis translation stage positioned in opposition to a second translation stage with an aluminum c-

channel extension positioned to press against the tip of the strain test plate (Figure 4-3). During experimentation, the test plate was strained normal to the face containing the embedded sensors by using the second stage to press the c-channel against the test plate. The test plate contacted the c-channel at 39mm from the fulcrum and was advanced in increments of 0.05mm using the precision micrometer on the stage. A Wheatstone-Bridge circuit was used to sense the change in resistance of the Omega strain gauge in real time during the testing using the conversion equation given by Omega as Equation 4-1 [20] where ΔR is the change in resistance of the strain gauge, R_0 is the initial, unstrained resistance of the strain gauge, and GF is the gauge factor for the strain gauge, as provided by the gauge specifications.

$$strain\ (\mu\varepsilon) = \frac{\Delta R \times GF}{R_0} \tag{4-1}$$

By displacing the tip of the test plate by 0.3mm, we achieved approximately 800 micro-strains within the test plate. A slight hysteresis was noted as the applied strain was released from the plate; however the increase in applied strain was essentially linear as expected (Figure 4-4). At each increment of deflection, 2000 spectra were recorded from each of the sensors and later post-processed to determine the optical path difference of the sapphire wafer in each sensor. The 2000 spectra were averaged in groups of 10, generating 200 data points for each level of applied strain. Figures 4-5 & 4-6 illustrate the wafer OPD as a function of applied strain; the 200 measurements are indicated for the two sensor geometries. Each sensor's OPD vs. strain response was quantified by linear curve fitting of the data obtained from the averaged spectra. From the curve fitting equations, it is evident that an increase in OPD with strain exists; however, as is shown in the following section, the effect of this strain cross-sensitivity is less than the temperature resolution of the sensor.

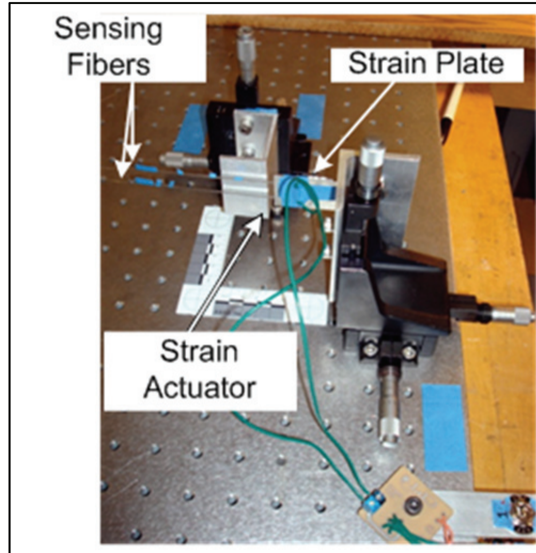

Figure 4-3: Strain cross-sensitivity testing apparatus

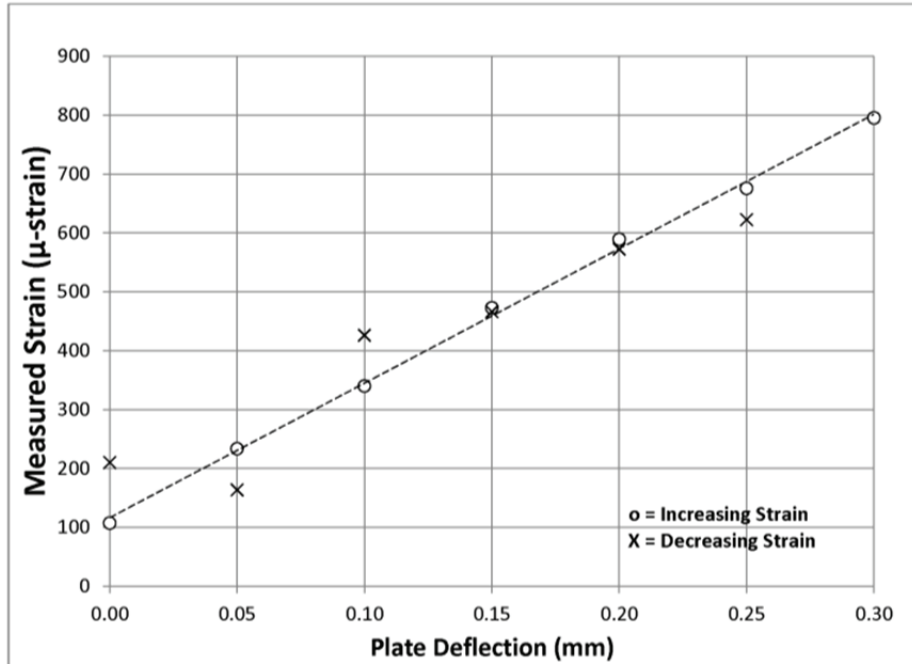

Figure 4-4: Plot of applied strain as a function of the deflection distance of the tip of the strain plate

In lieu of performing a full-scale temperature calibration for the sensors tested, a previously reported measurement of OPD vs. temperature sensitivity was used as a means for estimating the sensor response. Theoretical sensitivity of a sapphire wafer is dependent upon the thermal-optical coefficient ($\partial n/\partial T$), and the coefficient of thermal expansion, thus the previously reported sensitivity for a c-plane sapphire wafer should hold for these sensors as well. Zhu's work on surface mounted sapphire wafer temperature sensors [21] utilized sensing elements of

similar dimensions to those used in the strain experiments reported here, providing an acceptable analog for the thermal behavior of the sapphire wafers in the sensors. As is shown in the following figures, the OPD change as a result of strain is on the order of pico-meters per applied micro-strain (1.69 pm/με for the slot sensor and 0.48pm/με for the end sensor), as compared to the expected thermally induced OPD change reported by Zhu [22] of more than 1.5 nm/°C.

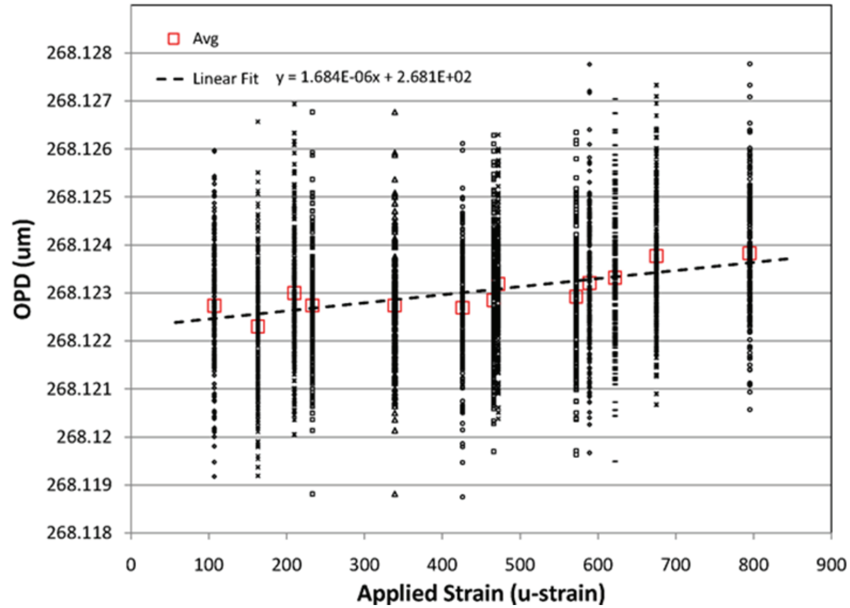

Figure 4-5: Optical path difference of slot sensor wafer etalon as measured at incremental applied strains

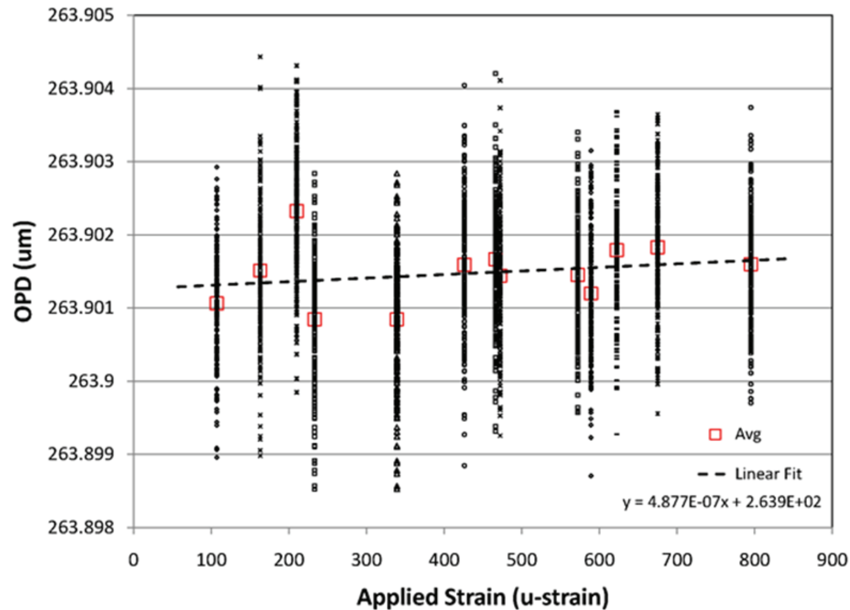

Figure 4-6: Optical path difference of end sensor wafer etalon as measured at incremental applied strains

4.1.3 Sensor Head Temperature Resolution

Performing a zero strain measurement and recording sensor spectra over several hours obtained each sensor design's temperature measurement resolution. The sensors were placed in a foam-insulated enclosure to isolate the effects of environmental temperature change. A two sigma measurement resolution of ±1.81°C for the slot sensor and ±1.77°C for the end sensor was calculated from the deviation of zero-strain temperature data. However, initial data revealed a periodicity in the OPDs of each of the sensors (Figures 4-7 & 4-8). It was determined that this periodicity was due to fluctuation of the ambient temperature in the lab area, despite the testing setup being shielded inside a foam enclosure. A further test was performed to correlate the temperature response of the sensors and verify that this was the cause of the periodicity.

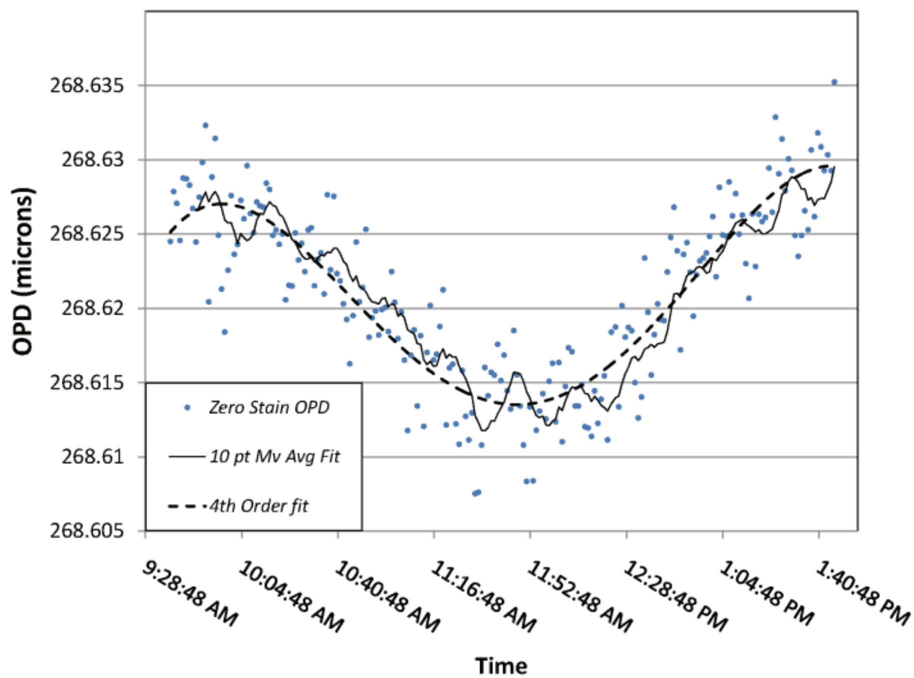

Figure 4-7: Variation in optical path difference of wafer etalon in slot sensor over time during a zero strain calibration run

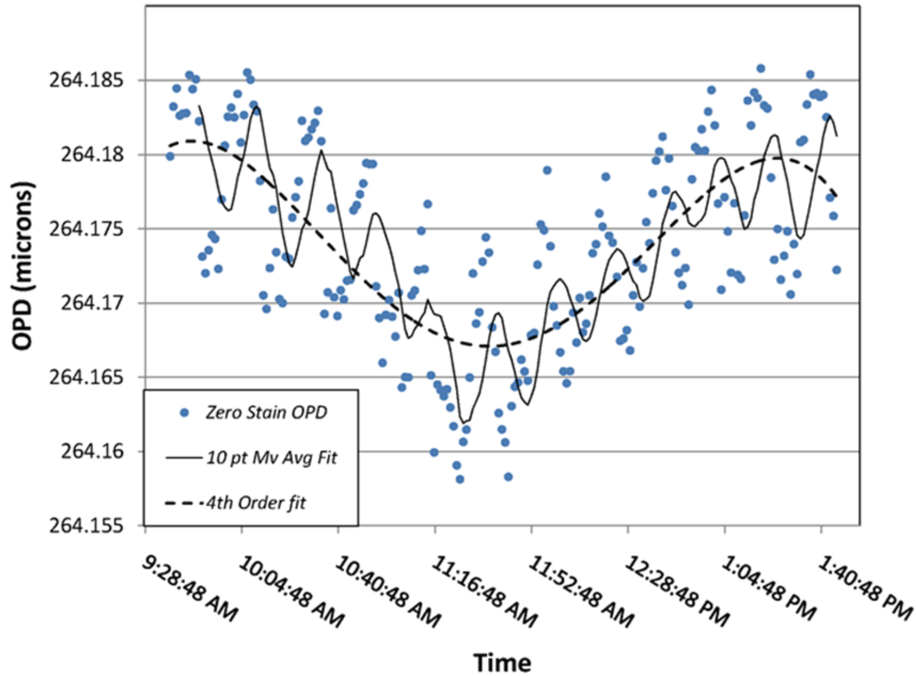

Figure 4-8: Variation in optical path difference of wafer etalon in end sensor over time during a zero strain calibration run

During the course of 10 hours, the sensor spectra from both sensors, and a temperature reading from an Omega k-type thermocouple seated adjacent to the test plate, were recorded. Figures 4-9 & 4-10 illustrate the result of this test and indicate a close correlation between the OPD of each sensor and the temperature recorded by the thermocouple. It should be noted that the thermocouple readout resolution is limited to 0.1°C, causing quantization of the temperature data in the graph.

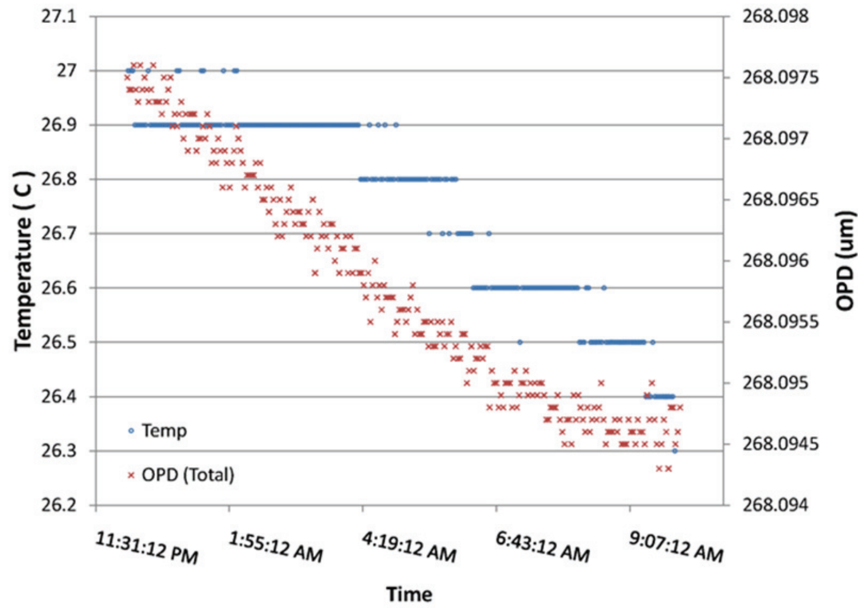

Figure 4-9: Variation in the recorded optical path difference of a slot sensor and thermocouple temperatures over time during a zero strain calibration run

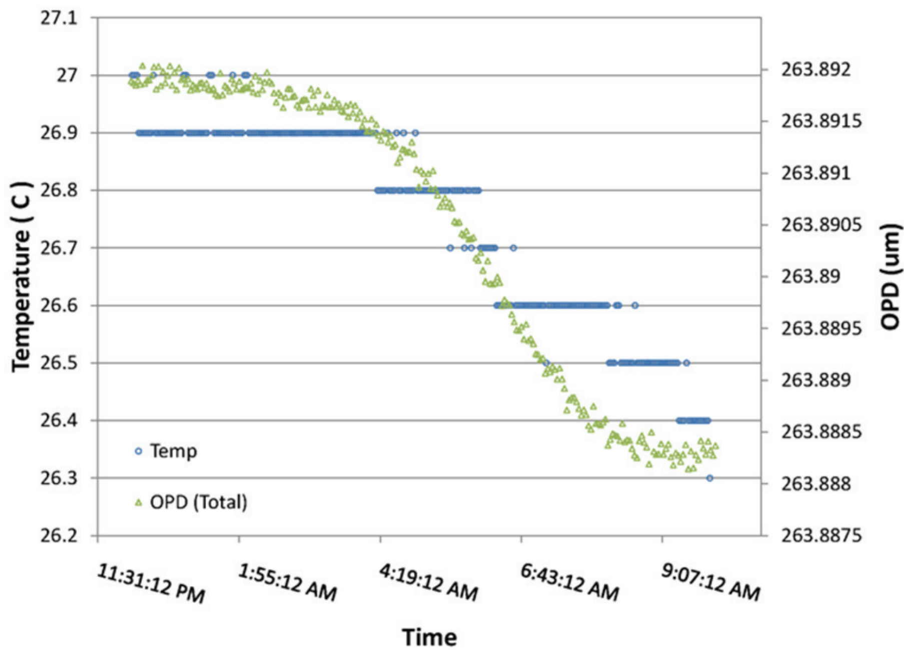

Figure 4-10: Variation in the recorded optical path difference of an end sensor and thermocouple temperatures over time during a zero strain calibration run

4.1.4 Strain Cross-Sensitivity Conclusions

To quantify each sensor's temperature-strain cross-sensitivity, the strain response of the wafer was converted into effective temperature measurement units. This provided a straightforward means to compare the effects of strain on the expected temperature measurement response and

resolution for the sensors. Zhu's reported OPD sensitivity change with temperature for ~60µm sapphire wafers of 1.524 nm/°C[5] was used for these calculations and the estimated sensitivity was then converted to the strain response of each sensor to the desired temperature units. The strain cross-sensitivity of the two sensors was found to be as follows in Table 4-2.

Sensor Type	Temperature Measurement Sensitivity (at 24°C)	Strain Cross-Sensitivity (w/ 95% confidence bounds)	Temperature Measurement Error at 1000µε
End sensor	1.524 nm/ °C	1.69 ±0.24 pm/µε	1.11 ± 0.06 °C/1000 µε
Slot sensor	1.524 nm/ °C	0.48 ±0.17 pm/µε	0.32 ± 0.04 °C/1000 µε

Table 4-2: Strain cross-sensitivity and calculated temperature measurement error for each sensor geometry

4.1.5 Adhesive Ferrule Design

As an offshoot of the end sensor design, the adhesive ferrule design was put forward as an alternative to a commercial ferrule option. In this design, the commercially available ferrule is replaced by a thin silica tube that was filled with ceramic following fiber positioning on a sapphire wafer. The intent was twofold; firstly, the diameter of the sensor head could be reduced by sing a tube with an OD in the range of hundreds of microns, thus minimizing the footprint of the sensor. Second, the fabrication of the sensor could be streamlined by affixing the fiber and wafer in an aligned state in a single step and eliminating the diameter mismatch between the ferrule and fiber that might allow the fiber and wafer to change alignment over time or due to mechanical shock. Figure 4-11 shows images of an adhesive ferrule sensor head constructed from gold coated silica fiber, a 20 mm segment of 850 micron OD x 700 micron ID silica tube, a 500x500 micron sapphire wafer, and Cotronics 989F alumina adhesive before and after addition of the ceramic adhesive. The alumina adhesive was found to significantly degrade the fringe visibility of the sensor on application, however after allowing he adhesive to air cure for several hours, the interference pattern was almost completely recovered (Figure4-12). Initial testing verified the feasibility of the design; however fabrication of the adhesive ferrule proved to be difficult to repeat. Further efforts were terminated in favor of nano-fabrication techniques that promised a significant decrease in overall sensor size.

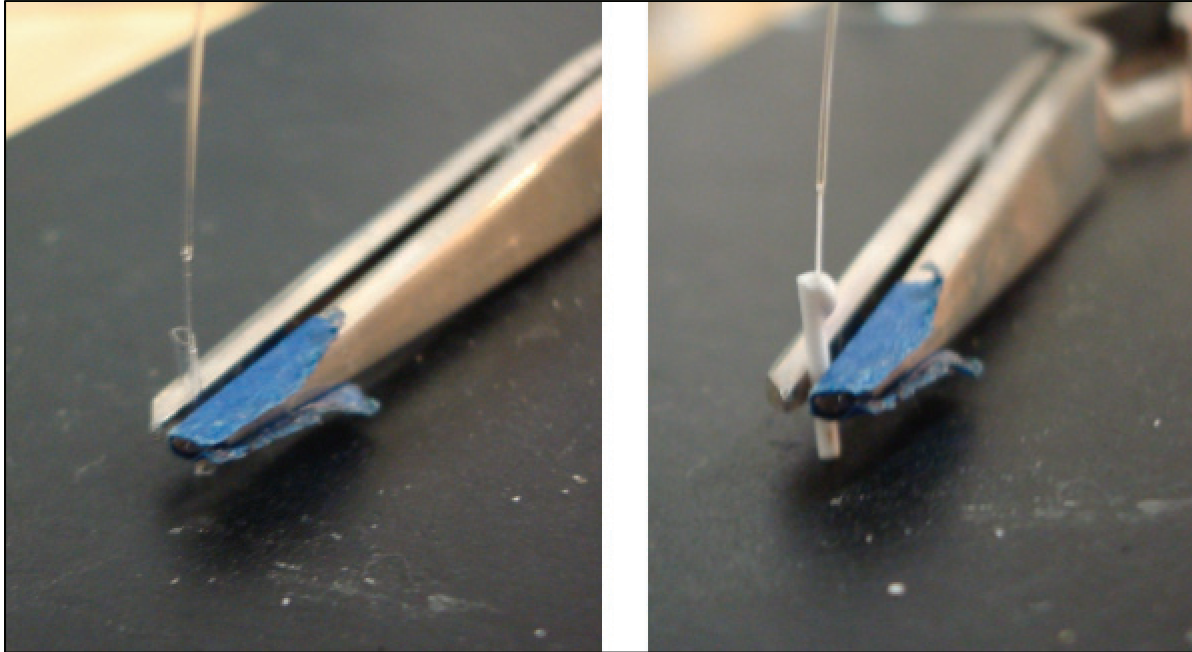

Figure 4-11: Images of a adhesive ferrule design sensor head before (left) and after (right) introduction of Cotronic 989F alumina adhesive to the silica tube

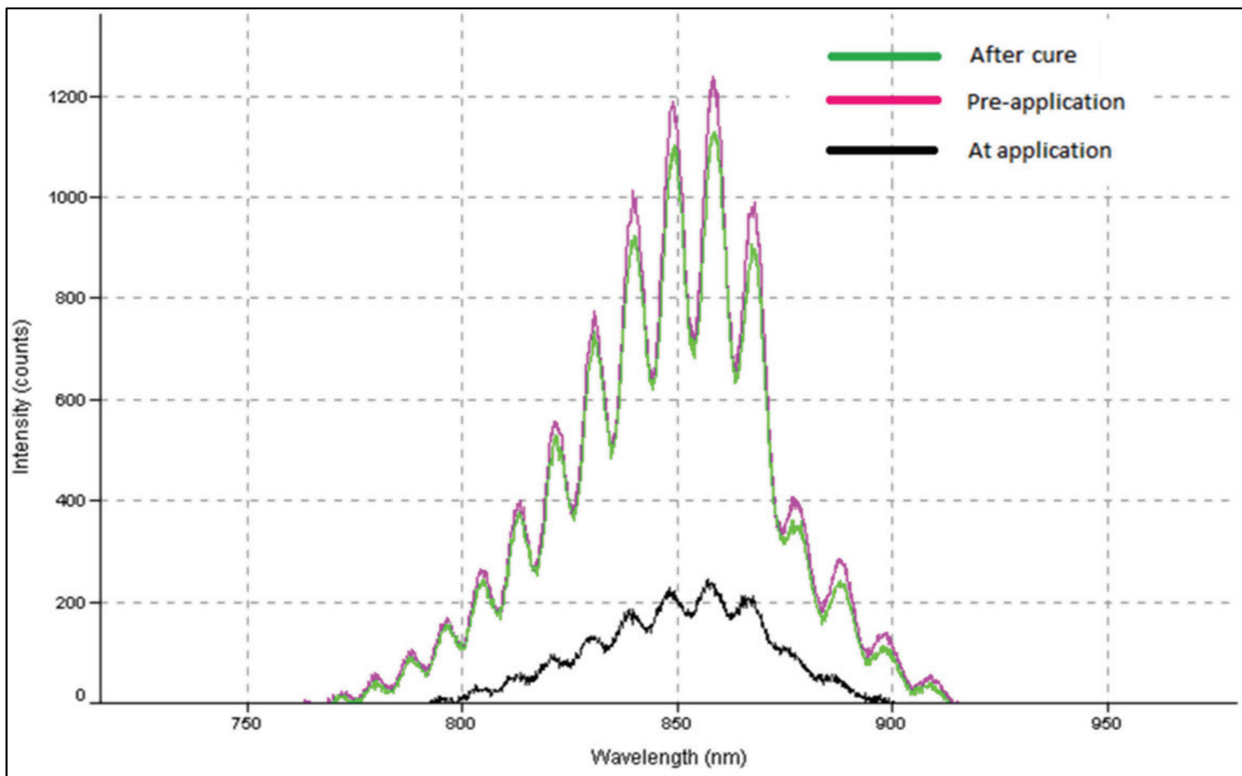

Figure 4-12: Optical interference patterns recorded for an adhesive ferrule sensor head prior to adhesive introduction, during adhesive curing, and after the adhesive has fully air cured

4.2 Focused Ion Beam Fabrication

Included in the specifications for the development of this system listed in Section 1.4 was Pratt & Whitney's requirement for a miniature sensor element. The quantitative goal for this requirement was to develop a sensor head with a major dimension of 1 mm or less. The designs discussed in Section 4.1 just meet this requirement, but refinement of the design was still desired. To that end, effort was put forth to decrease the size of the supporting structures involved in the wafer based etalon designs through minimization of ferrule dimensions and wafer size. While these efforts were valid, the possible reduction in sensor dimensions was limited.
Work being done concurrently with this project by Zhipeng Tian of the CPT with nano-fabrication techniques utilizing the Institute for Critical Technology and Applied Science's (ICTAS) Nanoscale Characterization and Fabrication Laboratory's (NCFL) FEI Helios 600 NanoLab Focused Ion Beam (FIB) apparatus to mill sapphire wafers inspired work which could reduce the size of the sensing element by an order of magnitude.

4.2.1 FIB Nano-fabrication Overview

The NCFL Helios Nanolab apparatus is a dual beam high vacuum instrument with a Scanning Electron Microscope (SEM) and Focused Ion Beam (FIB) utilizing a Gallium source. While the SEM is primarily an imaging tool, the FIB and be used for imaging as well as material removal and deposition on the nano-scale. The gallium ion beam is created by heating a gallium metal source and applying an electric field to form a point source on a tungsten needle, gallium ions are then siphoning off of the needle using an extraction voltage to accelerate the ions into the ion column through several magnetic lenses that accomplish beam focusing and rastering over the sample. The focused beam creates a spot size on the sample that is related to the beam current with a positive correlation. Higher beam currents will allow material to be sputtered from the sample's surface at a faster rate, but the spot size of the beam on the sample will necessarily be larger, thus reducing resolution. The process of interaction of the sample with the FIB results in the implantation of Gallium into the sample and is very destructive to the sample's surface. Imaging and material removal cannot be separated in this process, therefore surface examination by the FIB is generally performed at lower beam currents and over limited periods of time. Material deposition is also available using precursor gases. The interaction of the FIB with an injected precursor gas in proximity to the sample surface results in a chemical deposition of the

intended material. The NCFL contains precursor gases for platinum deposition as well as insulator deposition. Gas injection for selective etching is also available, as is a Xenon di-fluoride etch enhancement gas (XeF_2).

4.2.2 Wafer Milling

Tian's work focused on milling a pre-polished c-axis sapphire wafer to obtain a more streamlined shape for existing sensor head designs similar to those mentioned in Section 4.1, however the dimensions of the final wafer required manipulation and mounting within the FIB by qualified technicians. Additionally, the support and alignment features present in the wafer etalon design remained, thus continuing to keep the overall dimensions of the sensor head on the millimeter scale. To avoid these pitfalls attempts were made to fabricate wafers directly from sapphire fiber to create the smallest diameter wafer possible that would still cover the fiber tip. By using the FIB to mill the tip from the wafer, it might be possible to create the sensor head in situ without the need for additional manipulation following the milling procedure.

Sapphire fiber milling in the FIB required the fibers to be secured to a flat base after first polishing both ends of the fiber. One of the polished ends will create the far reflection surface of the EFPI etalon while the other required polishing in preparation for splicing to silica fiber for sensor interrogation. Working with sapphire in the FIB creates the issue of problems with electrical charging of the sapphire sample from the electron and ion beams. Due to the dielectric nature of sapphire (and the glass slide to which it was secured), there is no conductive path for the excess charge from the beams to reach ground. In order to mitigate this, graphite conductive tape was initially used to hold the fiber to the glass slide, however the removal process for the graphite tape formed a contamination on the fiber which proved extremely difficult to remove. In a fortunate occurrence, separate geology research being conducted at the same time had discovered that clear nail polish was also a conductive material, as well as having the favorable attribute of being easily dissolved in acetone with no residue left behind. Going forward, the clear nail polish method of affixing fibers for FIB work was used with great success. Prior to conducting the FIB work, the whole slide was sputter coated with a 5 to 10 nm layer of gold-palladium (Au/Pd) to form a conductive coating on the surface of the sample slide and fiber (Figure 4-13). The sample slide with attached fiber was mounted inside the vacuum chamber of the FIB also using conductive tape, and a strip of conductive tape was strapped from the top

Au/Pd coated surface to the metal structure of the sample stand to provide a grounding path for excess electrons to follow (for an example of this, see Figure 4-18 in Section 4.2.3.1).

Figure 4-13: Sputter coating glass slides with affixed sapphire fibers with gold-palladium ensures a conductive path to dissipate excess charge buildup during focused ion beam imaging and patterning

The first attempts at milling of the sapphire fibers were performed with an accelerating voltage of 20 kV and a beam current of 20 nA for the bulk cutting operations. The fiber was oriented on the slide so that the c-axis of the crystal lay perpendicular to the path of the ion beam. Automated cut completion time estimates were based on ion beam interactions with silicon, however work by NAME et al indicated that the milling of sapphire would require 5 times the dose or more to mill the same depth in sapphire. With this in mind the cutting parameters selected to sever the 75 micron fiber were the equivalent of a 750 micron cut in silicon. The milling geometry used was a 90 micron line cut with a beam width of approximately 70 nm. The time to complete this dose was 1 hour 48 minutes. On completion it was found that the fiber had not been severed and was still connected to the base fiber by a portion of sapphire at the bottom of the cut as shown in Figure 4-14.

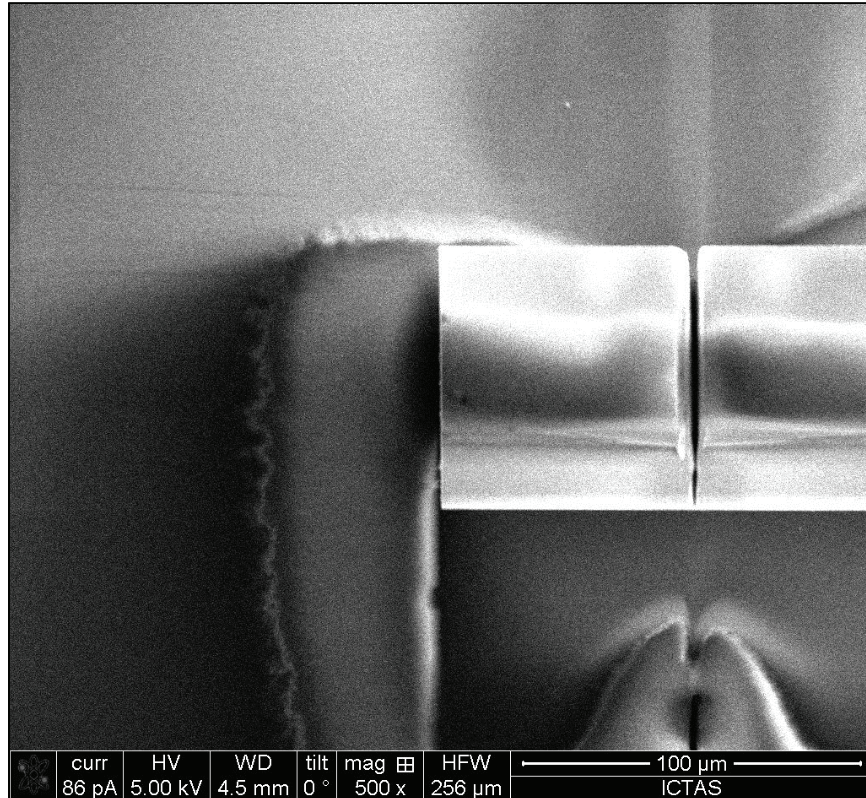

Figure 4-14: Secondary electron image of sapphire fiber that has been partially cut using the gallium ion beam

A cleaning cut was implemented in an attempt to both complete the separation of the fiber wafer and clean the upper surface of the fiber which had been chamfered by the Gaussian profile of the ion beam. The cleaning cut was performed at an accelerating voltage of 30 kV and a beam current of 9 nA. The cut parameters were for a 90 micron by 500 nm area to a depth of 80 microns, and the time to complete this dose was 48 minutes. The cleaning cut also did not result in a severing of the fiber wafer from the base fiber. The partially severed fiber wafer was secured to the base fiber using platinum (Pt) deposition to form reinforcing straps over the cut. Figure 4-15 shows an SEM secondary electron image of the Pt reinforcing straps and partially severed fiber wafer.

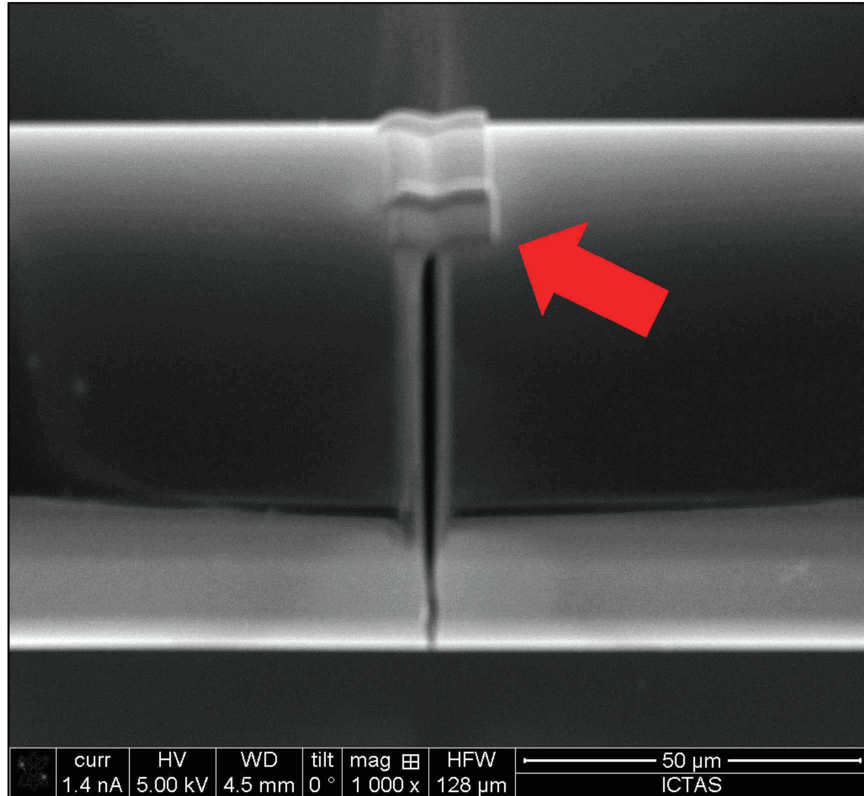

Figure 4-15: Secondary electron image of sapphire fiber milled with a gallium ion beam. The same ion beam was used with a platinum precursor gas to deposit reinforcing platinum over the gap left by the milling operation (red arrow indicates platinum deposition)

Further attempts to cut a fiber wafer by using similar cut parameters also failed to sever a fiber wafer from the base fiber. Analysis of SEM imagery of the attempts appeared to indicate that the ion beam was unable to clear the sputtered sapphire material from the depth of the cut, and once the beam had penetrated to approximately half of the diameter of the fiber, this material would become re-deposited within the cut and milling progress would cease. Figure 4-16 shows an optical microscope image through the end face of the sapphire fiber showing the ion beam cut. The arc of the cut is believed to be due to the re-deposition of material in the deepest part of the cut while areas nearer the circumference of the fiber were able to eject the sputtered sapphire and allowed the cut to remain clear. Additional efforts to cut a fiber wafer were also attempted using XeF2 etch assist gas injection at the cut site. The result of this effort was a threefold increase in milling time to reach the same result as previous attempts. The conclusion reached in these cases was that the XeF2 was effective in initial cutting of the sapphire material, however as the depth of cut increased, the interaction zone for the ion beam and XeF2 gas remained at the same position above the fiber's surface and worked to decrease the dose reaching the sapphire

material, thus negating any ability of the gas to increase ion yield from the sapphire and decreasing the overall material removal rate.

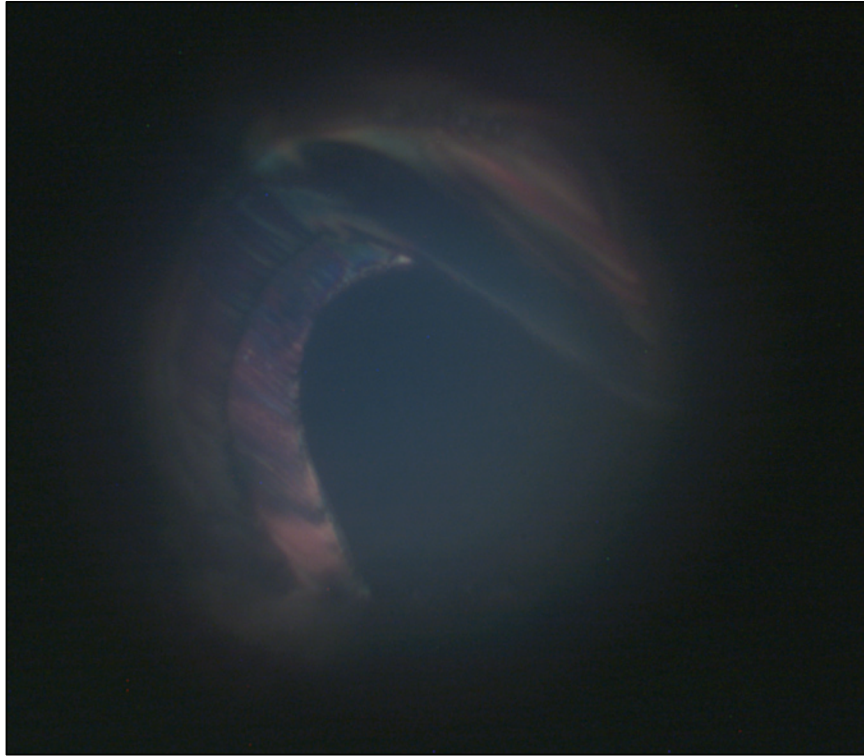

Figure 4-16: Optical microscope image taken through the base of a sapphire fiber that had been milled with a gallium ion beam in an attempt to sever 50 microns off of the end. The arc visible is uncut sapphire fiber and possible re-deposited sapphire material which was unable to be ejected during the milling process

4.2.2.1 Fiber Wafer Milling Conclusions

Given the re-deposition of amorphous sapphire material which occurred once the ion beam reached a cutting depth of approximately 40 microns it was determined that a line cut raster pattern of the ion beam would not provide sufficient clearance to allow ejection of the sapphire material from depth. A possible solution to this would be to raster the beam over a several micron wide rectangular area, rather than a 50 nm line-width, to allow space for the sputtered material to clear the cutting area prior to re-deposition. Unfortunately, given the considerable time and expense involved in performing a cut of such dimensions (likely to be on the order of 10s of hours) the idea was abandoned as infeasible. The experience gained while cutting the sapphire material was valuable in understanding the milling response of the ion beam perpendicular to the c-axis as opposed to milling on the c-plane of the sapphire. This experience is in sharp contrast to the milling operations detailed in the following section which utilize the c-place as the active cutting plane.

4.2.3 Nano-structure Cavities

Formation of an intrinsic Fabry-Perot interferometer (IFPI) in a sapphire fiber is a difficult proposition given the single crystal nature of the fiber. Currently there is no proven technique to establish the dielectric cavity within the crystal structure that would create the interferometer. Nano-fabrication, however, offered a means of creating a physical cavity within the fiber with optical quality surfaces. Additionally, the use of the FIB ensures the parallelism of the milled surface with respect to the initial surface by virtue of the incremental removal of material being constant over the pattern area sputtered by the ion beam.

4.2.3.1 Milled Cavity Interferometer

An attempt to create an IFPI in a sapphire fiber using nano-fabrication techniques centered on creating two reflecting planes at the fiber tip to form the interference cavity. Figure 4-17 illustrates the intended configuration in a cut-away view.

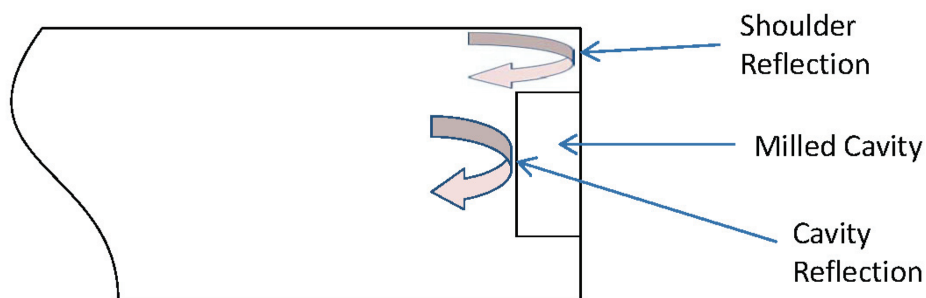

Figure 4-17: Schematic representation of fiber tip cavity sensor showing a cross section view of the cavity at the fiber's end

Several sapphire fiber tips were milled in the FIB by mounting them vertically in the vacuum chamber. Figure 4-18 shows vertically mounted sapphire fibers installed on the FIB stage with a piece of aluminum angle, and to the left a horizontally oriented slide with mounted fibers and wafers is visible.

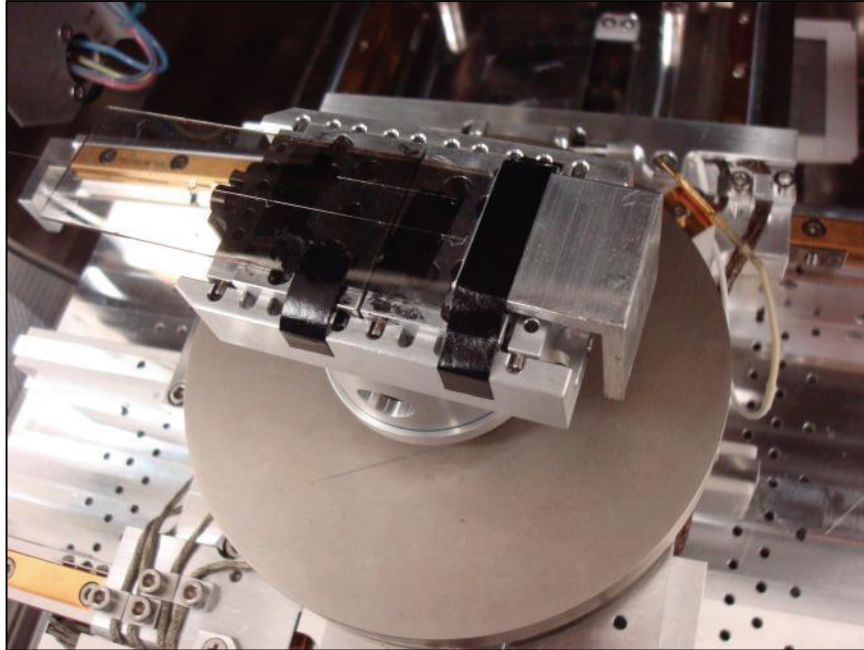

Figure 4-18: Sapphire fibers mounted on vacuum chamber stage prior to focused ion beam milling. A glass slide with fibers affixed horizontally and vertically oriented fibers affixed to the angle aluminum are visible in the image. Black graphite conductive tape spans both the slide and the aluminum to provide a grounding path

The use of double sided graphite tape to affix the aluminum angle was found to be inadequate to the task. During milling operations, the stage would be tilted to 52° in order to align the stage perpendicularly with the ion beam, as shown in Figure 4-19.

Figure 4-19: Helios NanoLab vacuum chamber internal camera image of stage tilted to 52 degrees

While tilted, the aluminum angle would sag on the tape under its own weight, causing the ion beam to drift off of the intended pattern at a rate of tens of nanometers per minute, effectively destroying the intended cavity structure. Figure 4-20 illustrates the consequence of the beam drift as a result of this movement. Further milling operations were completed using a fiber clamp created by Dr Brian Scott of the Materials Science Engineering department, shown in Figure 4-21, which was able to be fastened into the stage with a set screw to prevent unintentional movement during milling.

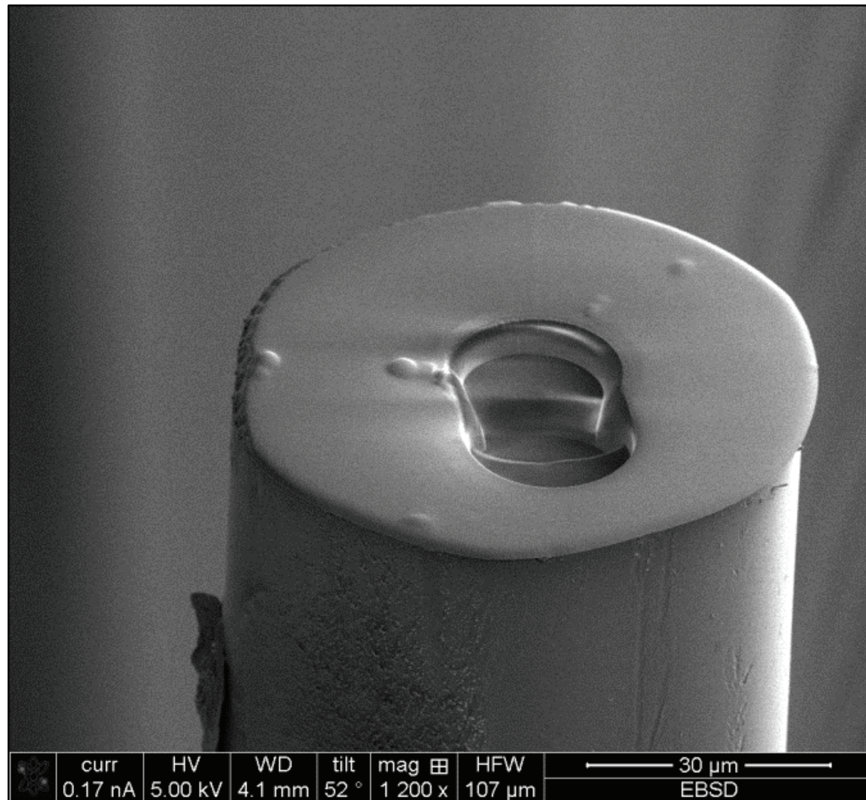

Figure 4-20: A sapphire fiber that was in the process of being milled when the aluminum angle sagged under its own weight and caused a shift in the pattern placement relative to the fiber tip

Figure 4-21: A fiber clamp fabricated by Dr. Scott is fastened into the translation stage via a set screw holding the clamp's post. Use of this clamp prevented movement of the fiber during milling operations

In contrast to the detrimental effects of XeF_2 assisted milling encountered during c-axis perpendicular milling, the gas was very effective in reducing cut times for c-plane milling operations. To ensure the quality of the sapphire surface created by milling with the ion beam, several sapphire wafers were milled with circular cavities that were then examined using an Atomic Force Microscope (AFM). An analysis of the mean surface roughness of cavities milled both with and without XeF_2 indicated that the milling operation preserved, and in some cases improved, the surface quality of the wafer, with mean surface roughness of less than twenty nanometers being typical. Figure 4-22 shows a three dimensional representation of the edge of a cavity milled into a sapphire wafer obtained with the AFM, and Figures 4-23 and 4-24 show optical and AFM topography images of the same cavity respectively.

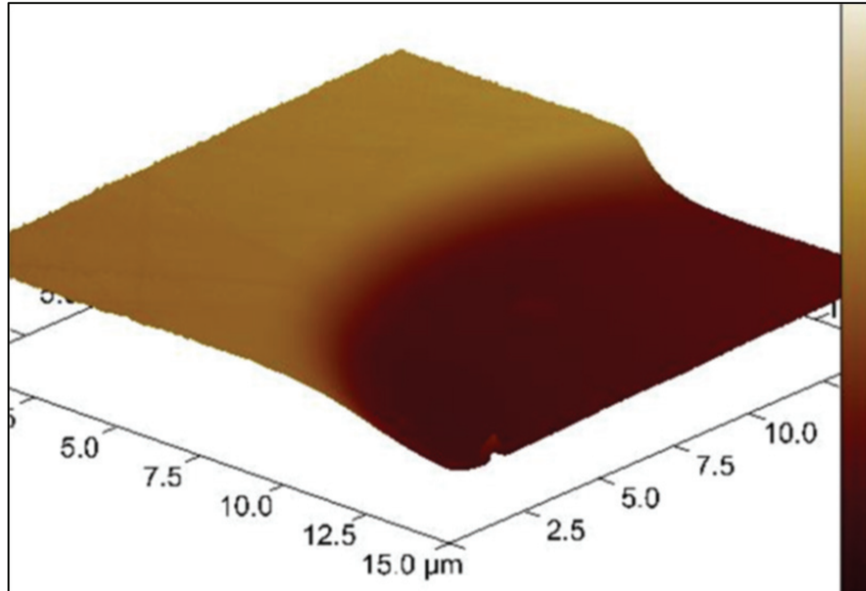

Figure 4-22: Three dimensional representation of wafer cavity edge imaged using an Atomic Force Microscope

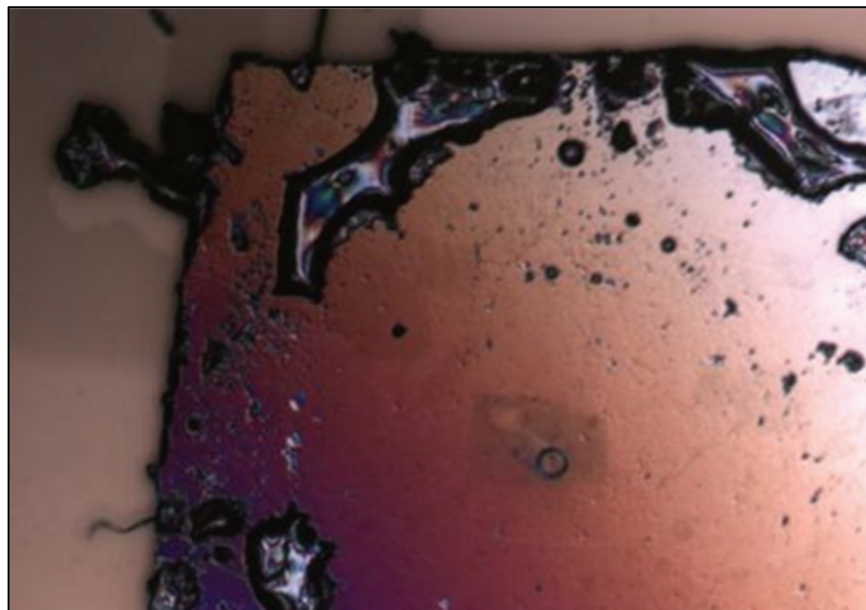

Figure 4-23: Optical image of cavity milled into a sapphire fiber using the ion beam. Cavity depth is approximate 1 micron and diameter is 20 microns

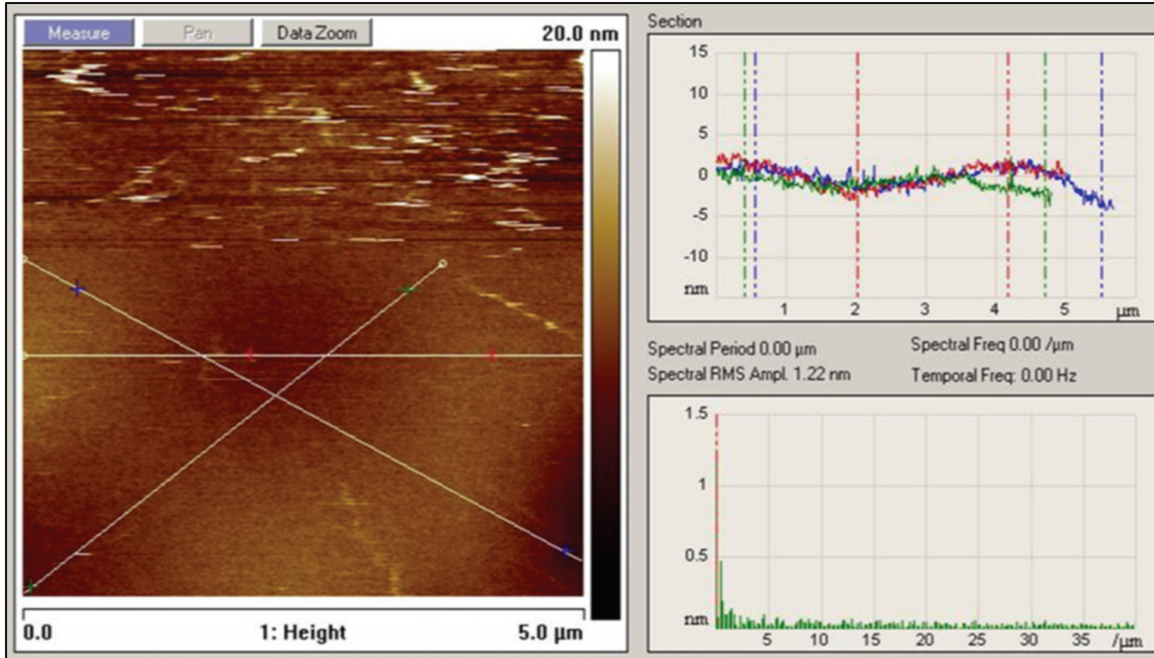

Figure 4-24: Atomic Force Microscopy topography map of center of a FIB milled cavity in a sapphire wafer. Milling depth was one micron

Figure 4-25 shows a secondary electron image of a typical fiber tip cavity milled into sapphire fibers used in this project. Of the sapphire fibers milled, the depth of the cavities was intended to be constant at approximately 10 microns deep with varying cavity diameters of 20 to 40 microns. As was covered in Section 3.2.3, a cavity length of 10 microns will not produce a sufficient number of fringes when interrogated with the 850 nm LED light source, therefore interrogation of these fiber tip sensors was conducted using a Super-Continuum light source, with a bandwidth of several hundred nanometers, and an Optical Spectrum Analyzer (OSA) with a wavelength range from 400 to 1700 nm. The fiber tip sensor interrogation system consisted of two configurations. In the first configuration, one of the fiber tip sensors was spliced to a 100/140 MMF pigtail and this pigtail spliced to a coupler attached to the light source and OSA in the same manner as the system described in Section 2.2. The second configuration utilized a quarter pitch graded index fiber (GIF) collimator to couple light from the silica MMF of the aforementioned coupler into the sapphire fiber tip sensors in lieu of attaching a silica pigtail fiber via fusion splicing. Initial interrogation attempts with one of the fiber tip sensors in the second system configuration appeared to show incipient fringes in the shorter wavelengths as shown in Figure 4-26, however this response was found not to be repeatable. It is now believed that the fringes were the possible result of spurious reflections creating a separate Fabry-Perot cavity and

not an interference pattern generated by the fiber tip cavity. Repeated interrogation of the sapphire fiber tip sensors with several additional configurations including using swept laser based optical spectrum analyzers and LED light sources with Ocean Optics spectrometers all failed to produce viable interference fringe patterns from the fiber tip sensors.

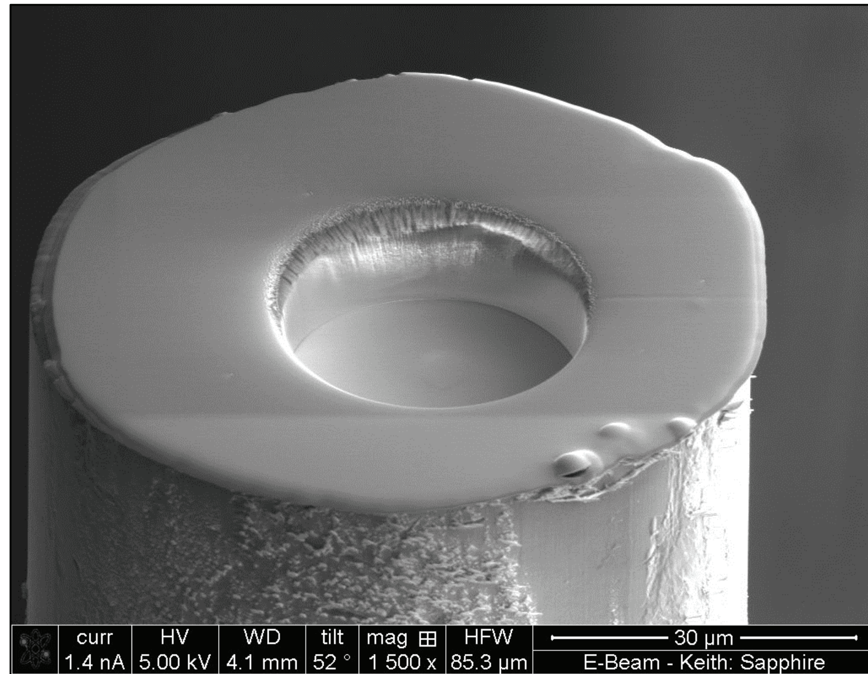

Figure 4-25: Secondary electron image of a 30 micron diameter by 12 micron deep cavity milled into the tip of a 75 micron diameter sapphire fiber

An analysis of the near field optical output of the milled fiber tips indicated that the diameter of the cavities was close to the optimal diameter to split the optical power evenly between the central cavity reflector and the shoulder reflectors of the fiber tip sensor, leading to a hypothesis that varying the interference cavity length might produce fringe patterns. To test this hypothesis, several silica fibers milled in the FIB to create cavities of varying depths between 14 and 60 microns. It was decided that silica would be used in place of sapphire to reduce the time required for fiber preparation, as the silica fibers could be cleaved rather than engaging in the time consuming sapphire fiber polishing process, and milling. Additional benefits of using silica fiber to create these test fiber tip sensors were the ease with which they could be spliced into an interrogation system, their greater flexibility and strength, and their cheaper material expense. Following the fabrication of these fiber tip sensors, each was interrogated using the same methods previously used on the sapphire fiber tip sensors with the same lack of results.

To rule out the possibility that the interrogation methods were to blame for the failure to obtain a signal from the fiber tip cavities, the milled fibers were used to guide light to glass cover slips and polished sapphire wafers in an attempt to obtain an interference pattern using these as the cavity. In every attempt a strong signal was obtained from the glass slide and sapphire wafer etalons indicating that the fiber tip cavity sensors were, in fact, the stumbling block. This result had the positive outcome of also indicating that the milled fibers were capable of guiding light to and from an external etalon.

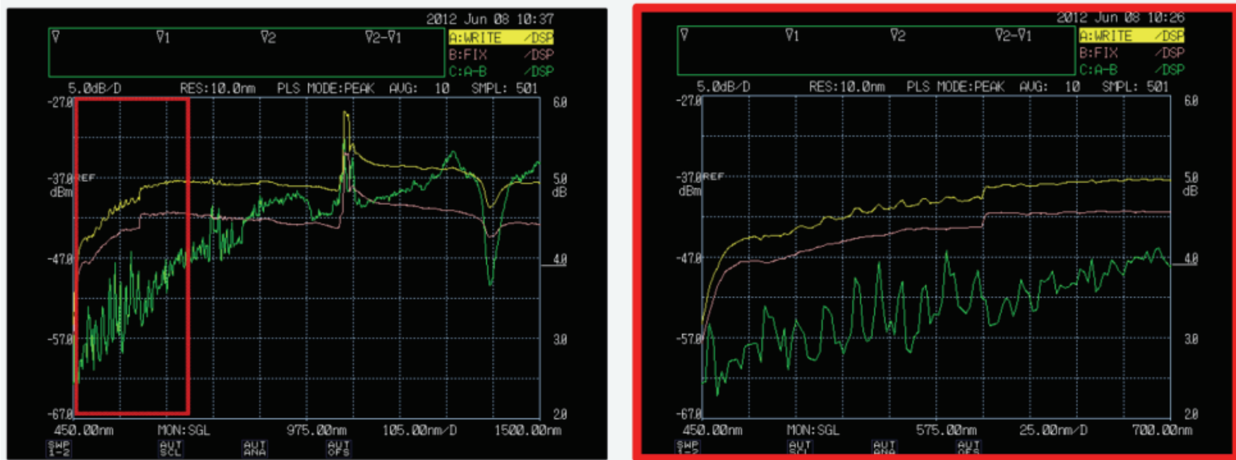

Figure 4-26: Optical spectrum captured by an optical spectrum analyzer formed by the interrogation of a 30 micron diameter cavity milled sapphire fiber illuminated with a Super Continuum light source. Right image is a zoomed in view of the red boxed portion of the spectrum shown in the left hand image

4.2.3.2 Modal Interference

Additional positive outcomes from the experiments detailed in Section 4.2.3.1 were the appearance of a second peak in the FFT of the interference pattern generated by interrogating sapphire wafers with the milled fiber tips, as is shown in Figure 4-27, and the appearance of a single peak when the milled fiber tip was pressed against a thick glass slide, as shown in Figure 4-28.The second peak in the sapphire wafer interrogations corresponded with the peak generated by the milled fiber tip in contact with the glass slide indicating that the cavity generated by the bottom of the milled cavity was creating a Fabry-Perot interferometer with the front surface of the sapphire wafer or glass slide.

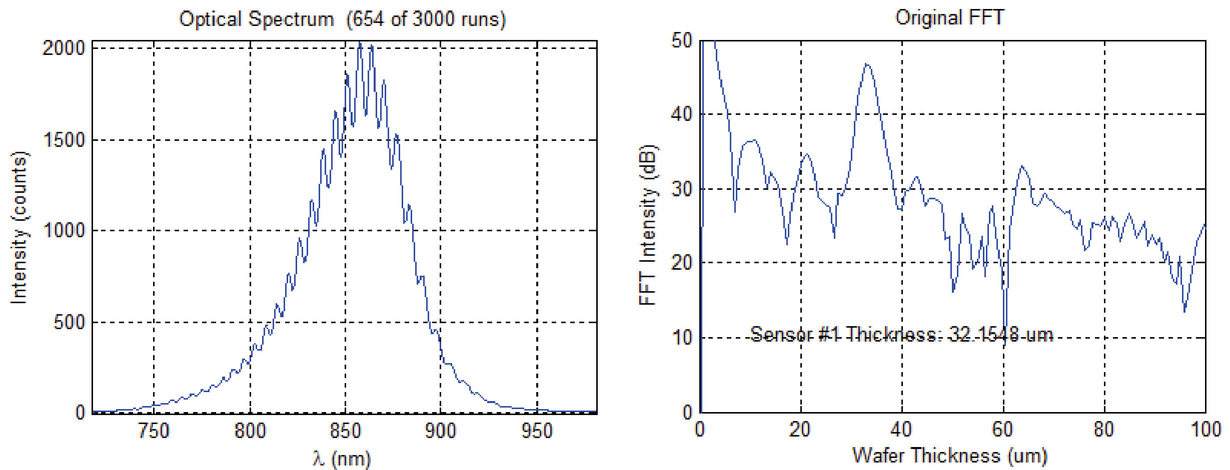

Figure 4-27: Optical interference spectrum (left) and corresponding Fourier transform (right) derived from the interrogation of a 32 micron thick sapphire wafer with a sapphire milled with a 30 micron diameter cavity of approximately 12 microns in depth

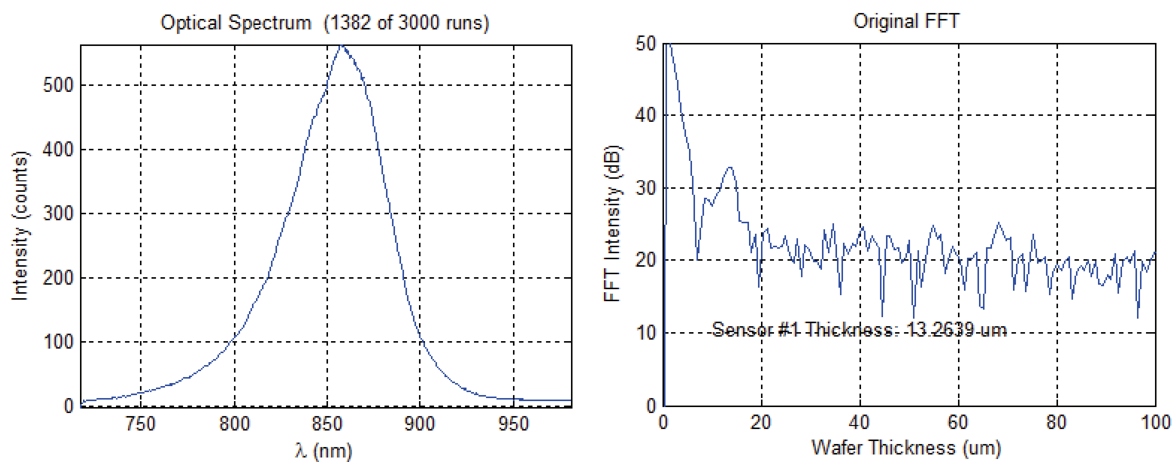

Figure 4-28: Optical interference spectrum (left) and corresponding Fourier transform (right) derived from the interrogation of a 1 mm thick glass slide with a sapphire milled with a 30 micron diameter cavity of approximately 12 microns in depth

This result also lent support to a developing hypothesis which explained the failure of the fiber tip cavities to generate interference patterns alone. Figure 4-29 illustrates a simplified ray trace of two modes in a milled MMF encountering the reflection surfaces of the milled cavity and fiber shoulder. The intent of this diagram is to indicate that the two surfaces will reflect different modes and that while the individual modes may interference, the number of modes encountering each is large and differential phase delay between a modes reflected from one surface and the other modes reflected from the other surface will average out the interference pattern and serve

to wash out the fringe visibility. It is the fact that the modes reflected by the surfaces are distinct that is believed to be the reason that no interference pattern is generated by the milled cavity.

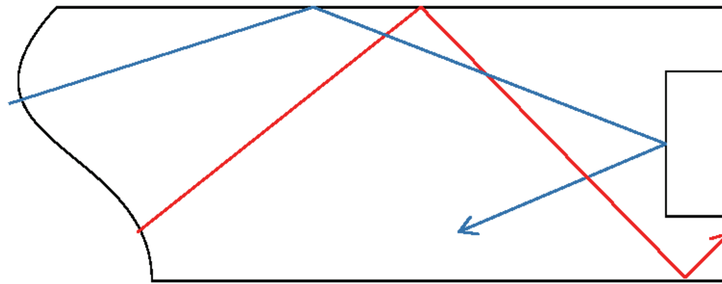

Figure 4-29: Ray trace diagram of a milled fiber tip's reflective surfaces with respect to two modes

In contrast, Figure 4-30 illustrates the case where the milled fiber tip is pressed against a thin sapphire wafer. As shown, modes which pass through the milled cavity will then encounter the front and the rear surface of the sapphire wafer and modes which encounter the shoulder can still pass into the wafer etalon. In the former case, an interference pattern will be generated by the distance between the cavity base and the wafer, in the second, an additional pattern will be formed by the wafer etalon. This result was repeated with a majority of the milled fibers. Of particular note is a silica fiber that had a milled cavity depth of greater than 60 microns (Figure 4-31). In this instance, no secondary peak was obtained in the FFT of the fiber tip on a thin wafer, and no peak at all was observed when the milled fiber tip was pressed against the thick glass slide. What was initially considered an anomalous result was then recognized to be the likely result of diminishing fringe visibility in the 60 micron cavity length range as determined by Han and discussed in Section 3.3.3.

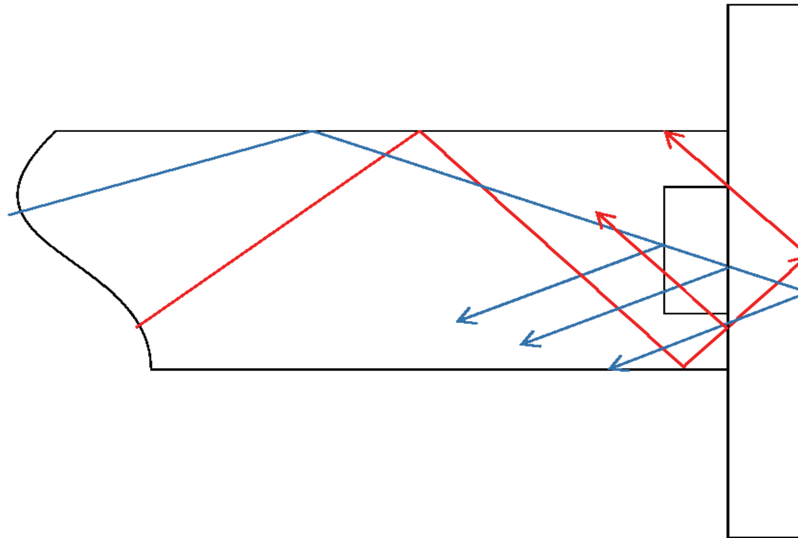

Figure 4-30: Ray trace diagram of two modes in a fiber with a milled tip used to interrogate a thin etalon

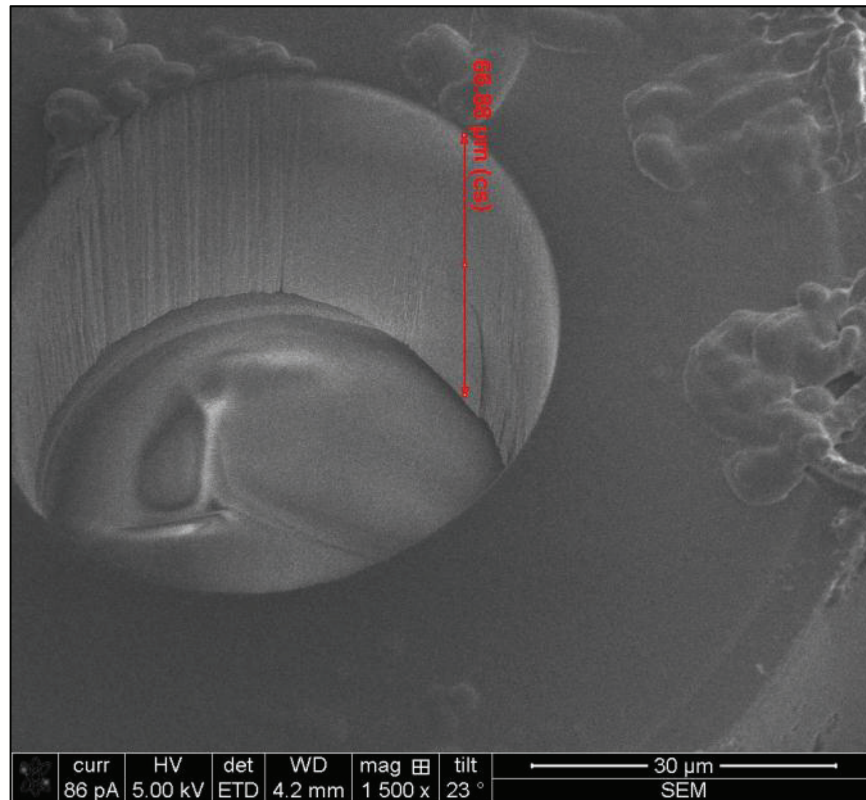

Figure 4-31: Secondary electron image of a deep cavity milled into a 100/140 multimode silica fiber using the ion beam

4.3 Direct Bonding of Sapphire Fibers

The ability of milled sapphire fibers to guide light like a standard fiber and provide an intrinsic secondary reflective surface is a favorable outcome of the project, however it does not, in itself,

advance the project's goals. Previous research done by Zhu et al. in 2006 [23] demonstrated a fiber tip pressure sensor created by selectively etching silica fibers. This pressure sensor was tested to 710°C with favorable results. The multiple cavity fringe demodulation demonstrated in the previous section with sapphire wafers and milled sapphire fibers opens the possibility of recreating Zhu's work with sapphire materials and potentially extending the operating temperature to 1600°C. Additionally, with the ability to create a flat bottomed cavity through FIB nano-fabrication, fringe visibility should increase substantially. Missing from the design, however, is a means of creating a hermetically sealed cavity from the milled fiber tip. Following on the work of Lally et al. [24], the prospect of creating this hermetic seal can be realized through direct bonding of sapphire substrates.

The process of direct bonding sapphire requires epitaxy-ready sapphire surfaces to be completely cleaned of contaminants and brought into contact at high temperatures. Using direct bonding, Lally et al were able to demonstrate a sapphire wafer pressure sensor [24] by applying differential pressure to the wafers during the pre and final bonding steps to create a bubble within the bonded sapphire. Use of FIB nano-fabrication to create a flat bottomed cavity in one or both of the wafers presents an opportunity for improvement on the demonstrated sensor, however the size of the sensor would still remain rather large. In an attempt to prove the concept on for a significantly smaller sensor, an experiment was carried out to perform direct bonding of two sapphire fibers.

The process to bond the sapphire fibers follows a previously developed process intended for the bonding of bulk sapphire [25]. The sapphire fibers to be bonded are prepared initially in by polishing the fiber ends to as smooth a surface as possible. The CPT has a fiber polishing apparatus that facilitates this process utilizing decreasing diamond grit pads down to 100 nm grit. Ideally the surface should be polished to better than single digit nanometer roughness to provide an epitaxy-ready surface. For this experiment, one of the sapphire fibers previously used in the fiber tip sensor experiments was utilized to provide a pressure cavity. A fiber alignment jig was designed and fabricated from low carbon steel and porous alumina to provide both alignment and clamping of the fibers. The intent of clamping the fibers was to maintain contact of the fibers by pre-loading them in the alignment ferrule with an axial force and holding that position. Figure 4- shows an image of the fiber alignment jig prior to use.

Cleaning of the fiber progressed from an acetone bath in an ultrasonic cleaner to acid cleansing first with NanoStrip solution and then a hot nitric acid bath. Following the cleaning, the fiber tips were subjected to a brief rinse with a dilute sulfuric acid solution to promote the formation of a hydroxide layer on the sapphire fiber tip surfaces (Figure 4-32). Following this rinse, the fibers were inserted into the alignment jig and clamped while being subjected to axial forces against one another. The clamped fibers were then inserted into a nitrogen flushed furnace for a 30 minute bake out at 200°C. The purpose of the initial bake out is to develop a preliminary hydrogen bond between the two fibers. After the initial bake out, the alignment jig was transferred to a furnace for an extended high temperature bake (1100°C for 50 hours) to facilitate the diffusion of atoms in the fibers across the contact interface of the two fibers and form the direct bond.

Figure 4-32: Fume hood set-up of Nano-Strip solution, hot nitric bath, and sulfuric acid wash in preparation for fiber cleaning in the Whittemore Hall clean room

Following the high temperature bake at 1100°C, the jig was removed from the furnace and inspected. The extended time at high temperature had accelerated the oxidation of the steel used in the jig (Figure 4-33) and necessitated a destructive disassembly of the jig to remove the fibers. Following removal it was found that the fibers had not succeeded in bonding to one another and the surfaces had remained pristine.

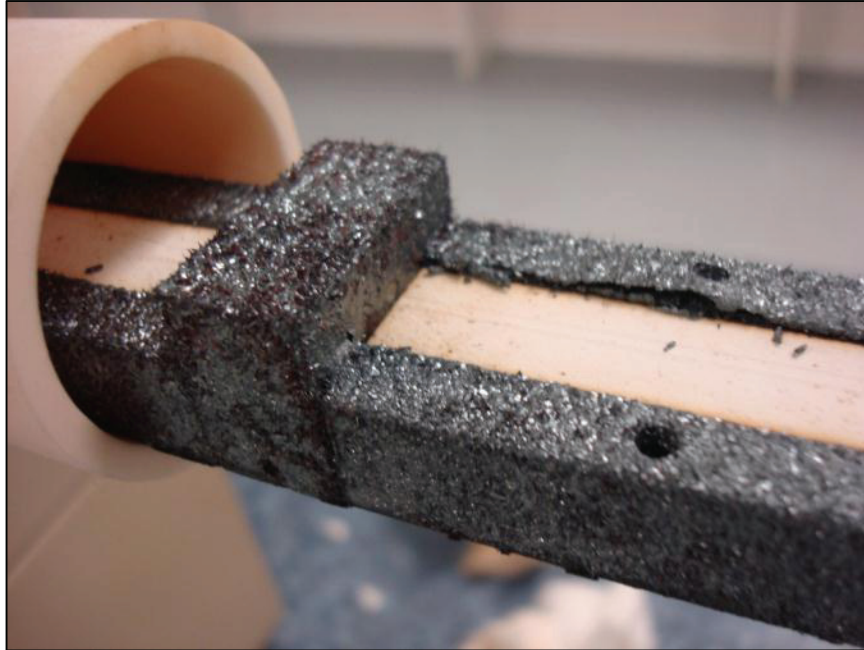

Figure 4-33: Excessive oxidation on low carbon steel components of alignment jig as a result of the high temperature bake

4.3.1 Direct Bonding Analysis

Visual inspection of the fiber tip surfaces following the direct bonding experiment revealed no signs that incipient bonding had occurred between the two fibers. The potential reasons for the failure of the fibers to bond range from inadequate surface quality of the fiber tips, contamination of the fiber tips, and misalignment of the fibers. The direct bonding procedure requires, at its heart, the intimate contact of sapphire surfaces. To accomplish this with two 75 micron fibers proved difficult even with the alignment jig. The central feature of the alignment jig was an alumina ferrule with an 80 micron ID. Given a 5 micron gap between the fiber and the inner wall of the ferrule, Figure 4-34 plots the potential misalignment of the fibers by location of the fiber mating point within the 10.5 mm long ferrule. As shown, the minimum misalignment that is likely to occur is approximately .3°. At this amount of misalignment, however the gap between the fibers is approximately 390 nm over the 75 micron diameter of the fiber. This distance is significantly larger than the atomic radius of aluminum at 1.43 angstroms and oxygen at 0.6 angstroms meaning that the atoms of the two fibers would likely be too far apart to facilitate diffusion. In addition to this, the oxidation of the alignment jig limited its use to a single experiment and required significant handling to disassemble. Had the bonding been successful, the disassembly process may well have broken the bonded fibers. Any future work in

this direction should include a more appropriate (in terms of materials and alignment procedure) and accurate means of bringing the fibers into, and maintaining, contact.

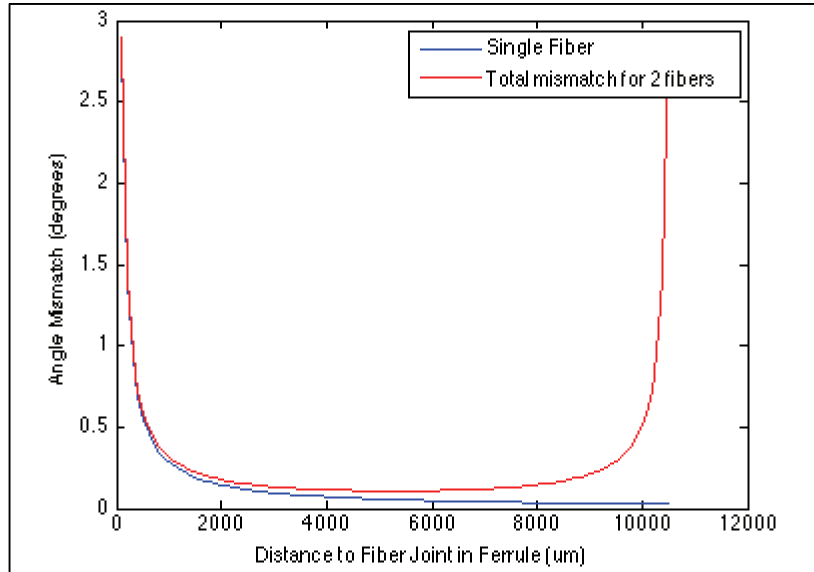

Figure 4-34: Plot of the estimated misalignment angle of fibers in direct bonding alignment jig as a function of joint position in the ferrule

Chapter 5: Sensor Multiplexing

5.1 Multiplexing the Wafer Etalon Design

As mentioned in Section 1.3, the initial specifications set forth by Pratt & Whitney for the sensor project called for a semi-distributed sensor configuration. In practice, a semi-distributed configuration refers to a string of discrete sensing points rather than a continuously sensed region. To accomplish this requirement, the wafer etalon design was fabricated to allow for inline multiplexing of additional sensors by means of the slot sensor design. Figure 5-1 illustrates a cutaway view of the multiplexed sensor elements.

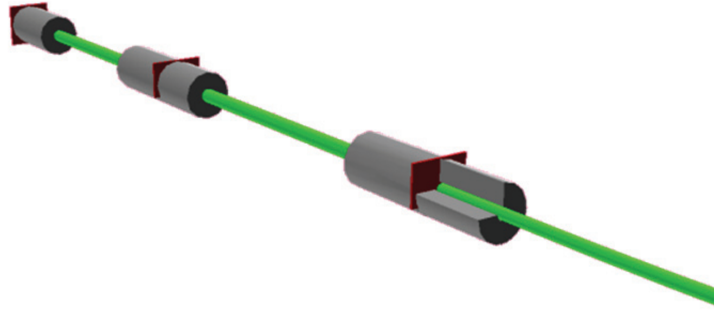

Figure 5-1: Cutaway representation of a multiplexed 3 sensor link of sapphire wafer sensing elements

Assembly of the three sensor link was accomplished using multiple three axis stages to manipulate custom fabricated ferrule holders and sapphire fibers. Figure 5-2 shows a completed three sensor link utilizing two slot sensors and a single end sensor. Demodulation of the three sensor link is accomplished in the same fashion as a single wafer etalon demodulation following on work completed by J. Wang et al. [26]. The ability to resolve three sensors proved difficult as the third sensor's SNR was consistently lower than that of the first two (Figure 5-3). While the multiplexed sensor link work was abandoned in favor of research efforts centered on reducing the individual sensing element footprint, it is now believed that the cavity length used in the end sensor contributed to the weaker signal, as the thickness of the sapphire wafer falls into the low FV regime identified by Han, et al, and discussed in Section 3.2.2.

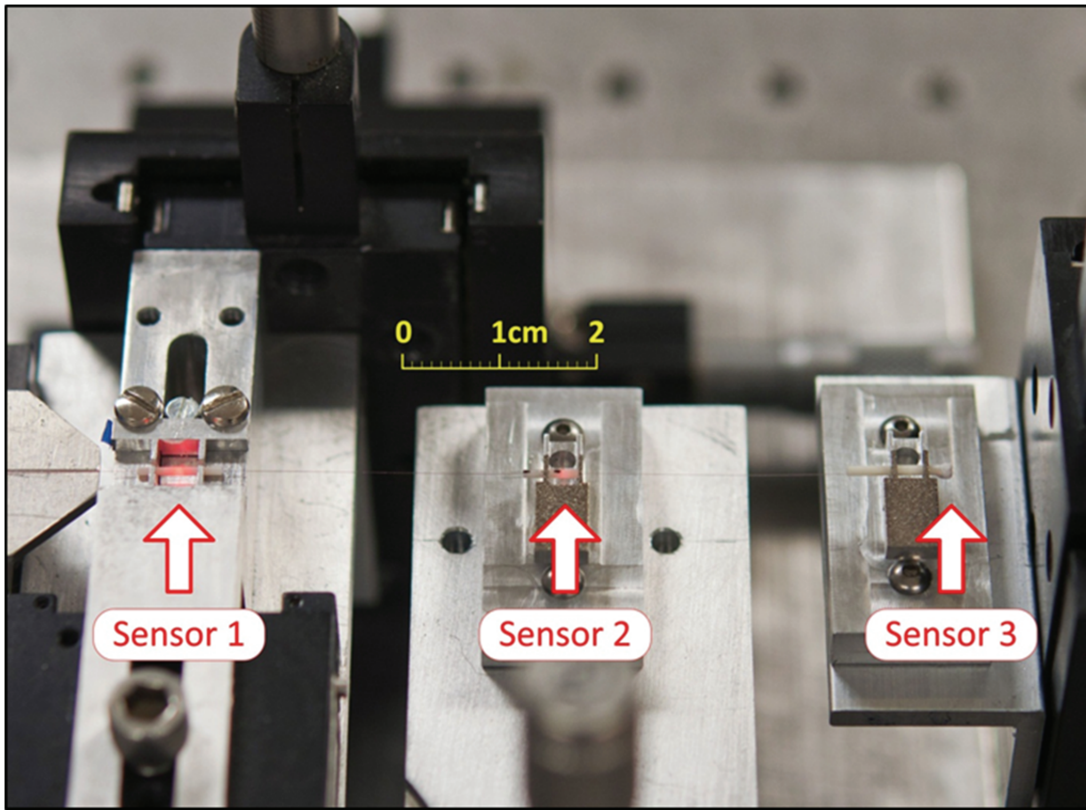

Figure 5-2: A multiplexed 3 sensor link of sapphire wafer sensing elements illuminated with a 630 nm laser

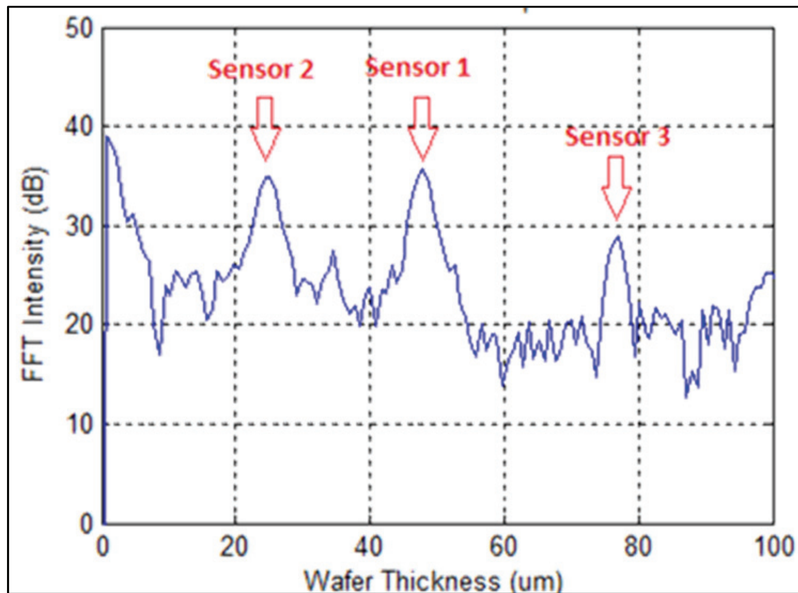

Figure 5-3: Plot of the Fourier transform derived from the combined interference pattern generated by the three wafer etalons in a multiplexed sensor link

Chapter 6: Summary and Recommendations for Future Work

6.1 Work Summary

The refinement of a wafer based EFPI temperature sensor enabled the CPT to meet the specifications set forth by the project sponsors in achieving a multiplexed high temperature sensor capable of resolving three distinct points while utilizing a single egress fiber. The use of sapphire, alumina, and zirconia components will allow the sensor to operate in high temperature environments of up to 1600°. Strain testing provided solid evidence of the low cross-sensitivity between strain and temperature exhibited by the wafer etalon design utilized in the sensor's fabrication. Efforts to reduce the size of the sensing elements by an order of magnitude through the use of nano-fabrication techniques proved moderately successful and opened directions of research for the fabrication of sapphire based fiber tip temperature sensors as well as the possibility of a combined fiber tip pressure and temperature sensor.

6.2 Recommendations for Future Work

The miniaturization and simplification of the wafer etalon based thermometer remains as an area ripe for improvement. It is believed that continued work with direct bonding of sapphire substrates can accomplish the bonding of two sapphire fibers and form the precursor to a fiber tip sensor with sub millimeter dimensions. FIB based nano-fabrication techniques have also been applied to distributed sensing along a sapphire fiber through frequency domain reflectometry work currently being conducted by CPT researchers, and continued advancement of the techniques with regard to sapphire and silica substrates is recommended.

Continued work on implementing the multiplexed wafer etalon sensor link in a field testable package is also indicated, however advancement of the direct-bonded sensor element would obviate the need for wafer based sensing elements altogether.

References

[1] D. DeWitt, Theory and Practice of Radiation Thermometry, New York: Wiley, 1988.

[2] Z. H. F. S. a. A. W. Yizheng Zhu, "Sapphire-fiber-based white-light interferometric sensor for high-temperature measurements," *Optics Letters,* vol. 30, no. 7, pp. 711-713, 2005.

[3] National Instruments, "Thermocouple Accuracy Table by Type and Temperature," National Instruments, 2 June 2007. [Online]. Available: http://digital.ni.com/public.nsf/allkb/776AB03E065228408625727B00034E20. [Accessed 15 August 2012].

[4] I. Forest M. Mims, Light-Beam Communications, Indianapolis: Howard W. Sams & Co., 1975.

[5] Corning, "Corning ClearCurve multimode optical fiber," 1 January 2011. [Online]. Available: http://www.corning.com/WorkArea/showcontent.aspx?id=36549. [Accessed 15 March 2011].

[6] J. C. Palais, Fiber Optic Communication, Upper Saddle River, NJ: Pearson Prentice Hall, 2004.

[7] Temperatures.com, "Resistance Sensors (RTDs)," 1 November 2012. [Online]. Available: http://www.temperatures.com/sensors/csensors/resistance-temperature-detectors-rtds/. [Accessed 5 August 2012].

[8] J. S. S. &. I. D. Aggarwal, Infrared Fiber Optics, Boca Raton: CRC Press LLC, 1998.

[9] B. A. Chuck W. Schietinger, "Reliability improvement methods for sapphire fiber temperature sensors," in *Fiber Optics Reliability: Benign and Adverse Environments IV*, San Jose, 1990.

[10] H. L. D. T. S.G. Lipson, Optical Physics, London: Cambridge U.P., 1995.

[11] B. Z. a. M. Hahrizi, "High-Temperature Resistance Fiber Bragg Grating Temperature Sensor Fabrication," *IEEE Sensors Journal,* vol. 7, no. 4, pp. 586-591, 2007.

[12] M. H. a. A. Wang, "Exact analysis of low-finesse multimode fiber extrinsic Fabry-Perot interferometers," *Applied Optics,* vol. 43, no. 24, pp. 4659-4666, 2004.

[13] A. W. Gary Pickrell, "Single-Crystal Sapphire Optical Fiber Sensor Instrumentation:

Topical Report," DOE Award Number: DE-FC26-99FT40685, Pittsburgh, 2009.

[14] F. S. a. A. Wang, "Frequency-estimation-based signal-processing algorithm," *Applied Optics,* vol. 44, no. 25, pp. 5206-5214, 2005.

[15] B. D. J. G. a. A. W. C. Ma, "Decoding the spectra of low-finesse extrinsic optical fiber Fabry-Perot interferometers," *Optics Express,* vol. 19, no. 24, pp. 23727-23742, 2011.

[16] P. Ewart, "Optics," University of Oxford, Oxford, 2008.

[17] G. Ivanov, *Fabry-Perot Sapphire Temperature Sensor for Use in Coal Gasificaton,* Blacksburg: Virginia Tech Thesis, 2011.

[18] R. K. N. a. J. A. Harrington, "Optical properties of single crystal sapphire fibers," *Applied Optics,* vol. 36, no. 24, pp. 5934-5940, 1997.

[19] H. X. B. R. a. Y. Z. Eric J. Ruggiero, "Decoupled Temperature and Strain Measurements using Fiber Bragg Grating Sensors," in *Photonic Fiber and Crystal Devices: Advances in Material and Innovations in Device Applications II*, San Diego, 2008.

[20] Omega Engineering, Inc, "Strain Gage Technical Data," 1 January 2010. [Online]. Available: http://www.omega.com/techref/strain-gage.html. [Accessed 12 November 2010].

[21] Y. Z. a. A. Wang, "Surface-mount sapphire interferometric temperature sensor," *Applied Optics,* vol. 45, no. 24, pp. 6071-6076, 2006.

[22] Y. Zhu, *Miniature Fiber Optic Sensors for High-Temperature Harsh Environments,* Blacksburg: Virginia Tech Dissertation, 2007.

[23] K. L. C. G. R. P. a. A. W. Yizheng Zhu, "High-Temperature Fiber-Tip Pressure Sensor," *Journal of Lightwave Technology,* vol. 24, no. 2, pp. 861-869, 2006.

[24] Y. X. A. W. Evan M. Lally, "Sapphire direct bonding as a platform for pressure sensing at extreme high temperatures," in *Fiber Optic Sensors and Applications VI*, Orlando, 2009.

[25] H. F. T. S. T. A. A. Sugiyama, "Direct bonding of Ti:sapphire laser crystals," *Applied Optics,* vol. 37, no. 12, pp. 2407-2410, 1999.

[26] B. D. E. L. M. H. a. A. W. J. Wang, "Multiplexed high temperature sensing with sapphire fiber air gap-based extrinsic Fabry-Perot interferometers," *Optics Letters,* vol. 35, no. 5, pp. 619-621, 2010.

This page intentionally left blank